

PPPL-5268

## Remote Temperature Sensing for Scanning Auger Microprobe

A. M. Lewis, C. H. Skinner

July 2016



Prepared for the U.S. Department of Energy under Contract DE-AC02-09CH11466.

# Princeton Plasma Physics Laboratory

## Report Disclaimers

---

### Full Legal Disclaimer

This report was prepared as an account of work sponsored by an agency of the United States Government. Neither the United States Government nor any agency thereof, nor any of their employees, nor any of their contractors, subcontractors or their employees, makes any warranty, express or implied, or assumes any legal liability or responsibility for the accuracy, completeness, or any third party's use or the results of such use of any information, apparatus, product, or process disclosed, or represents that its use would not infringe privately owned rights. Reference herein to any specific commercial product, process, or service by trade name, trademark, manufacturer, or otherwise, does not necessarily constitute or imply its endorsement, recommendation, or favoring by the United States Government or any agency thereof or its contractors or subcontractors. The views and opinions of authors expressed herein do not necessarily state or reflect those of the United States Government or any agency thereof.

### Trademark Disclaimer

Reference herein to any specific commercial product, process, or service by trade name, trademark, manufacturer, or otherwise, does not necessarily constitute or imply its endorsement, recommendation, or favoring by the United States Government or any agency thereof or its contractors or subcontractors.

---

## PPPL Report Availability

### Princeton Plasma Physics Laboratory:

<http://www.pppl.gov/techreports.cfm>

### Office of Scientific and Technical Information (OSTI):

<http://www.osti.gov/scitech/>

---

### Related Links:

[U.S. Department of Energy](#)

[U.S. Department of Energy Office of Science](#)

[U.S. Department of Energy Office of Fusion Energy Sciences](#)

# Remote Temperature Sensing for Scanning Auger Microprobe

A. M. Lewis<sup>1</sup>, C. H. Skinner<sup>2</sup>

<sup>1</sup>Department of Mechanical, Aerospace and Nuclear Engineering,  
Rensselaer Polytechnic Institute, Troy, NY 12180, USA

<sup>2</sup>Princeton Plasma Physics Laboratory, Princeton, NJ 08542, USA

Liquid lithium is being studied for potential application as a plasma-facing material in tokamaks. This research focuses on an experiment designed to study the temperature dependence of lithium wetting, a process that is important for the application of lithium on tokamak walls. This paper describes the calibration of the infrared pyrometer that will be used in a scanning Auger microprobe to measure the temperature of the lithium sample. An effective emissivity value was used to correct for factors, other than temperature, that affected the pyrometer reading. The ZnSe lens and vacuum viewport were found to significantly decrease the effective emissivity, as did colder objects in the field of view. The field of view of the pyrometer was measured to be 0.6 cm in diameter, and the effective emissivity was found to decrease slightly as the scanning Auger microprobe sample holder temperature increased.

## I. INTRODUCTION

Lithium conditioned plasma facing surfaces have enhanced plasma performance on many fusion devices and liquid lithium plasma facing components are under consideration for future machines [1]. A key factor in the performance of liquid lithium components is the wetting by lithium of its container. Studies by Klein et al [2], have shown that ultra-thin wetting layers of Sn may form on polycrystalline Al surfaces at room temperature under ultra-high vacuum (UHV) conditions if material reservoirs are present. Liquid metal wetting has also been investigated by Saiz et al [3], who report on the fundamental differences between the mechanisms controlling spreading of organic liquids and liquid metals and on formation of Marangoni films driven by surface-tension gradients in high-temperature systems. The spreading of lithium on stainless steel was observed via scanning electron microscopy (SEM) and elemental imaging using scanning Auger microscopy (SAM) in a Thermo Scientific Microlab 310 F Scanning Auger Microprobe and Microanalysis instrument [4]. The results showed that solid lithium can wet a stainless steel surface at room temperature by emitting a thin layer that spreads away from a Li island on the surface. The process by which this solid metal wetting occurs is not yet well understood and experiments at elevated temperatures are planned using a heatable sample holder.

The temperature of the Li sample will be measured by an infrared pyrometer, due to the impracticality of incorporating a thermocouple and readout connection in the current sample holder in the SAM while it is under vacuum. The pyrometer requires calibration, however, to account for transmission losses at the vacuum chamber viewport and lens, potential cold materials within the field of view of the pyrometer and the sample emissivity. To minimize the time spent with the SAM UHV chamber at atmosphere the factors involved in the calibration were initially investigated on the bench and then the final calibration was performed with the SAM at atmosphere. Section II explains the factors that affect the pyrometer reading. Section III describes the bench calibration setup and equipment used. Section IV presents the measurements done on the effects of the ZnSe lens and viewport on the field of view and Section V discusses the measurements of the dependence of emissivity on temperature. Section VI describes the measurements done on the field of view of the pyrometer, and Section VII discusses the *in-situ* calibration in the SAM.

## II. FACTORS AFFECTING THE PYROMETER READING

The pyrometer reading represents the average temperature of the objects within its field of view and this may include objects with different temperatures and/or emissivity values. Transmission losses in the ZnSe viewport and lens will also affect the temperature reading. The transmission of ZnSe between 1  $\mu\text{m}$  and 20  $\mu\text{m}$  is about 70% and drops off sharply outside of that range [5]. The pyrometer uses a version of the Stefan-Boltzmann equation, Eq 1, to calculate the temperature from the net thermal power that it measures. An additional factor,  $\alpha$ , in the equation can be used to account for all of the other factors that affect the pyrometer reading.

$$I \left[ \frac{\text{W}}{\text{m}^2} \right] = \alpha \epsilon \sigma (T^4 - T_a^4) \quad (1)$$

Here  $I$  is the net thermal power,  $\sigma$  is Stefan's constant ( $5.670 \times 10^{-8} \text{ W/m}^2\text{K}^4$ ), and  $T_a$ , the ambient temperature, is measured with a sensor in the pyrometer. The emissivity,  $\epsilon$ , is the ratio of the object's thermal emission to that of a black body. Emissivity values between 0.1 and 1.0 can be manually input to the pyrometer [6]. Figure 1 shows the digital readout of the pyrometer. The value of  $\alpha\epsilon$ , which is here referred to as the effective emissivity, is input into the pyrometer in order to obtain a temperature reading that matches the temperature measured by a thermocouple temporarily attached to the sample.

## III. EXPERIMENTAL SETUP FOR BENCH CALIBRATION

The pyrometer used is an Omega OS552A (-1 FOV) Infrared Pyrometer, which has a digital readout and removable alignment laser. Figure 2 shows the body and lens of the pyrometer and the optical axis, with the removable alignment laser in dashed lines. The laser alignment system consists of a coaxial class 2 laser pointer that can be used to determine the approximate location of the optical axis of the pyrometer. The laser attachment, however, must be removed when measurements are made, as it obstructs the field of view of the pyrometer. The field of view of the pyrometer varies slightly with distance from the pyrometer lens and the nominal spot diameter, at 90% energy, is 0.9 cm at a distance of 61 cm [6].

A biconvex ZnSe lens of focal length 50 cm with an antireflection coating ( $R_{\text{avg}} \leq 0.5\%$  @ 7.5 – 13.5  $\mu\text{m}$ ) [4] reduced the operating distance of the pyrometer to 34 cm, close to the 40 cm distance from the pyrometer to the sample in the SAM geometry. The pyrometer views the sample inside the SAM through a ZnSe vacuum viewport. The SAM geometry with the ZnSe

lens and viewport was replicated in the bench calibration. A calibrated Omega HH12B Type K thermocouple was used to independently measure the temperature of the heated object. The thermocouple junction was in physical contact with the object, and the reading served as a reference temperature. The calibration of the thermocouple was performed using ice water and boiling water. The thermocouple temperature reading for the ice water was 0.5°C, and for the boiling water 99.5°C, indicating that the thermocouple is accurate to within a half a degree over that range of temperatures.

Figure 3 illustrates the dependence of the pyrometer temperature reading on the input effective emissivity, and importance of having the correct emissivity setting. The data was recorded by manually changing the emissivity values and the points have been fit with a b-spline using Origin 6.1 software.

The first object used to study the effects of the ZnSe lens and viewport was a black coffee mug. The projected surface area of the mug, 71 cm<sup>2</sup>, was much larger than the field of view of pyrometer (estimated to be 0.27 cm<sup>2</sup> at a location 40 cm from the pyrometer lens) and so the mug fully filled the field of view at all distances that were used in these tests. The setup is shown in Figure. 4(a).

Secondly, a Digital 01833 soldering iron with temperature adjustable up to 430°C was used. The soldering iron was aligned with the optical axis of the pyrometer, with the thermocouple leads physically attached to the tip. The setup of the soldering iron tests is shown in Fig 4(b).

The third object was the sample holder to be used in the SAM. This is a cm-scale stub with a carbon tape cover, which for these tests was mounted on a Line Tool Model A Micropositioner. The micropositioner allowed the stub to be moved in all three dimensions with thousandth of an inch accuracy. The stub was placed so that the optical axis of the pyrometer was incident on the center of the stub face. Measurements were done with the stub face 30° from the optical axis, Fig. 4(c), and 60° from of the optical axis, Fig 4(d). In the SAM, the stub face will be 30° from the optical axis, and the 60° tests were done to provide more information about the field of view effects. The sample holder was heated electrically using a GW Instek PSP-2010 power supply.

#### IV. ZnSe TRANSMISSION LOSSES

The ZnSe lens and viewport were each aligned to ensure that they were perpendicular to and centered on the optical axis of the pyrometer laser alignment system. The location of the laser spot without the lens or viewport was marked, and the lens and viewport were each inserted and aligned so that the laser spot returned to this location. The ZnSe transmission losses were then studied by measuring the apparent temperature of a mug and a soldering iron. The coffee mug tests were performed by filling the mug with hot water (initial temperature 47°C) and placing it in the field of view of the pyrometer. The emissivity setting in the pyrometer was then manually adjusted until the temperature reported by the pyrometer matched the thermocouple temperature. This setting was the effective emissivity of the mug. The measurement was first done with just the mug, then repeated after the ZnSe lens had been inserted and aligned, and then repeated again after the ZnSe viewport was inserted and aligned. The initial temperature reading of the pyrometer decreased with each insertion. The effective emissivity for just the pyrometer and mug was  $\epsilon = 0.82$ , decreased to  $\epsilon = 0.78$  with the addition of the lens, and decreased again to  $\epsilon = 0.70$  with both the lens and the viewport. The larger effect of the viewport is attributed to the lack of an anti-reflective coating. Figure 5 shows the difference between the pyrometer and thermocouple readings for the three cases in this test: the mug alone, the mug and lens, and the mug, lens and viewport.

A soldering iron was used for calibrations at higher temperatures. The projected area of the iron seen by the pyrometer was  $0.2 \text{ cm}^2$ , smaller than the field of view of the pyrometer, and so these measurements were sensitive to the colder objects behind the iron as well as to temperature inhomogeneities in the iron and its alignment. The location of the laser spot relative to the pyrometer optical axis was determined by removing the laser attachment and shifting the soldering iron until the pyrometer reading reached its maximum.

The iron was first heated to 430°C, and the effective emissivity found to be  $\epsilon = 0.45$  without the lens or viewport. To study the temperature dependence of the effective emissivity with the ZnSe optics, the pyrometer readings were recorded between 30 °C and 400 °C for the three cases studied in the mug tests—the iron alone, the iron and lens, and the iron, lens and viewport. In each case, the iron was heated for six minutes, and then allowed to cool in the air. The temperature readings from the pyrometer (with emissivity setting of  $\epsilon = 0.45$  for all cases) and thermocouple were recorded every fifteen seconds for the first two minutes, then every thirty

seconds between two and ten minutes, and every minute for the rest of the fifteen minute experiment. Figure 6 shows the results of this test. The differences for all three cases tend towards zero as the temperature reaches room temperature because the pyrometer uses the net power (above room temperature thermal radiation) to calculate the temperature. However, the percent difference between the thermocouple and pyrometer temperatures increases in magnitude at lower temperatures. The effect of the ZnSe viewport was much larger than the effect of the lens, in accordance with the mug tests. The effect of the lens is almost negligible, which we attribute to the transmission loss being compensated by the change in the field of view. Figure 7 shows the relative sizes of the iron tip and the field of view. The field of view with the lens is significantly smaller than without the lens, so the colder objects behind the iron (the wall, soldering iron holder, etc) had less of an effect on the pyrometer temperature reading.

## V. EMISSIVITY

Potential changes in the emissivity with temperature were studied with the soldering iron. The soldering iron was heated to 400°C, and the effective emissivity was found to be  $\epsilon = 0.51$ . This was higher than the value found in the previous soldering iron tests because of a change in the location of the iron and the objects in the background. The iron was approximately five inches closer to the pyrometer in this test to reduce the influence of the background objects on the results. The difference between the pyrometer and thermocouple readings was recorded for several emissivity settings over the range of temperatures between 30°C and 400°C. The iron temperature was reduced by lowering the set heating temperature until a new stable temperature was established. At each setting, the pyrometer and thermocouple temperatures were recorded for each of the emissivity settings. The first set of emissivity values used was 0.47, 0.49, 0.51, 0.53 and 0.53, but as the temperature decreased, so did the effective emissivity, and so at lower temperatures measurements at emissivity settings of 0.40 and 0.35 were also taken. Figure 8 shows the results of this test, with the data points fitted to b-splines using Origin 6.1 software. Where each line crosses zero on the y-axis (the point at which the pyrometer and thermocouple temperatures are equal) is the temperature at which that emissivity setting is the effective emissivity of the setup. The effective emissivity decreased from 0.50 to 0.40 as the temperature decreased from 400° to 50°C.

## VI. FIELD OF VIEW

The soldering iron was replaced by the SAM sample holder for the subsequent measurements. The location of the laser spot on the sample holder relative to the optical axis was measured by removing the laser attachment and shifting the sample holder until the pyrometer reading reached its maximum. The laser attachment was then put back on the pyrometer and the location of the laser spot with respect to the sample holder recorded, as shown in Figure 9. The laser spot was found to be approximately 5 mm below and 2 mm to the left of the center of the pyrometer optical axis. The field of view of the pyrometer, lens and viewport setup was measured using an aluminum 1 mm diameter aperture just in front of, but thermally isolated from the sample holder, as shown in Figure 4(d). The sample holder was at a 30° angle to the optical axis of the pyrometer. The sample holder was moved across the optical axis both horizontally and vertically and the pyrometer readings were recorded for each location. The pyrometer emissivity was set to  $\epsilon = 0.84$ , the literature emissivity of the black carbon tape covering the sample holder surface<sup>[7]</sup>. The fact that most of the field of view was filled with the room temperature aluminum (which has a much lower emissivity) lead to the measurement of unrealistically low temperatures. Figure 10 shows the results of this test. The temperature readings along the vertical centerline, shown in Figure 11, were used to estimate the field of view. The criterion from the pyrometer manual, 90% of the max energy, was used and the field of view was found to be 0.7 cm in diameter at a location 40 cm from the pyrometer front face.

The dependence of the field of view size on the distance from the pyrometer was then measured using the sample holder at both 30° and 60° angles from the optical axis, without the 1 mm aperture. For each distance from the pyrometer lens the sample holder was moved horizontally across the optical axis at a fixed vertical position. Figure 12 shows the distribution of pyrometer temperature readings for the 60° angle, and Figure 13 for the 30° angle. There was no significant dependence of the field of view with distance from the pyrometer over the range 24 – 32 cm within the step size (0.635 cm) of the measurements. The pyrometer emissivity was set to  $\epsilon = 0.84$  for both measurements. The maximum pyrometer temperature reading for the 60° setup was higher than the 30° setup as the 30° setup filled less of the field of view. Figure 14 shows the field of view with the projected area of the sample holder at each angle.

The temperature distribution over the face of the sample holder was measured using the sample holder at a 30° angle from the optical axis and the 1mm diameter aperture, however this time the aperture was stationary and centered on the optical axis of the pyrometer. The sample holder was placed behind the hole and moved horizontally and vertically across the optical axis. Figure 15 shows the pyrometer temperature reading distribution from this test. The temperature readings again unrealistically low because of the aluminum aperture. The temperature variation of 3°C was within the experimental error and hence not significant.

Future experiments will use a small metallic Li sample mounted on the carbon tape. The effect of a metallic Li sample on the effective emissivity was estimated using small tabs of 316-stainless steel that were placed on the sample holder surface. The metal tabs had a room temperature emissivity of  $\epsilon = 0.3$ [8] and reduced the effective emissivity of the sample holder setup. The effective emissivity of the sample holder with each tab was found by varying the pyrometer emissivity setting until the pyrometer and thermocouple readings matched. For this test, the average thermocouple temperature reading was 114°C. Figure 16 shows the difference between the pyrometer reading and thermocouple reading as the emissivity value in the pyrometer was varied for each metal tab. Figure 17 shows, for each measured value of the percent of the surface covered, the ratio of the effective emissivity to the effective emissivity of the setup with no metal. The points were fit to a curve, Eq. 3, which can be used to calculate the effective emissivity of the sample holder with a metal sample at any temperature by multiplying the effective emissivity with no metal by the ratio found using Eq 2.

$$R(p) = a + be^{-cp} \quad (2)$$

In Eq. 2,  $R$  is the ratio of the emissivity to the emissivity with no metal on the surface,  $p$  is the percent of the surface that is covered in metal, and the value of  $a$  is  $0.428 \pm 0.009$ , the value of  $b$  is  $0.570 \pm 0.008$  and the value of  $c$  is  $0.031 \pm 0.008$ .

## VII. SAM CALIBRATION

The pyrometer was installed on the SAM such that the pyrometer optical axis passed through the center of the sample holder surface as determined using the laser alignment system taking account of the offset discussed in Sect. VI. The ZnSe lens was aligned and bolted into place in front of the pyrometer lens. The thermocouple leads were attached to the sample holder,

and the Instek power supply was used to electrically heat the sample holder. The black carbon tape was removed from the sample holder because of outgassing concerns, and the surface was painted with special low-outgassing black paint instead to achieve the higher emissivity desired.

The relationship between the temperature of the sample holder and the current was found using the thermocouple for several values of the current up to 3A and is shown in Figure 18. The equilibrium temperatures for those current values were fit to a curve, Eq 3, shown in Figure 19. The dependence of the effective emissivity on the temperature of the sample holder is shown in Figure 20. The effective emissivity at each temperature was found by varying the emissivity setting to find the setting at which the pyrometer and thermocouple readings matched and is shown in Figure 20. The points were fit to a curve, Eqs 3 and 4, which represents the relationship between the effective emissivity and the sample holder temperature. The values for the constants in these two fits are given in Table 1. The uncertainty in some these parameters is very large, because the data points do not fit a simple shape very well. This uncertainty leads to large uncertainties on the final values calculated.

$$T(I) = Y + \left(\frac{V}{k}\right) (1 - e^{-kI}) \quad (3)$$

$$\varepsilon(T) = aT^b \quad (4)$$

---

**Table 1. Coefficient Values for Temperature and Emissivity Fits**

---

<u>Coefficient</u>	<u>Value</u>
Y	19 ± 6
V	-17 ± 4
k	-0.7 ± 0.1
a	0.186 ± 0.008
b	0.114 ± 0.009

---

These two fits were used to find the relationship between the effective emissivity and the current. This relationship is shown in Figure 21, represented by the black line denoted “0%”. The label indicates that this is the relationship for the effective emissivity when there is no metal on the surface of sample holder. The uncertainties in the measured quantities and the fit coefficients were propagated through Eqs 3 and 4 to produce the uncertainties shown in the upper plot of

Figure 22. The lower plot shows the uncertainty in the actual pyrometer temperature reading if the suggested emissivity setting is used. This plot was generated by propagating the emissivity setting uncertainty through Eq 1. The propagation of the uncertainty in the temperature reading was split into two terms, the uncertainty contribution from the emissivity setting, and the contribution from all other sources. The contribution from all other sources was assumed to be the uncertainty that is given in the manual for the pyrometer reading (3°F or 1% of the temperature reading, whichever is larger). This resulted in the second plot of Figure 22. The uncertainty in the temperature reading is dominated by the second term, the contribution from the pyrometer itself, while the uncertainty in the emissivity setting has a relatively small effect.

Equation 3 was then used to determine the relationship between the emissivity setting and current if a percentage of the surface of the holder is covered in metal. The relationship was found for four distinct percentages: 1%, 5%, 10% and 15%. This was done by combining equations 2, 3 and 4. The relationships for all four values can be seen in Figure 21. As was done for the case with no metal on the surface, the uncertainties are shown in separate plots. Figures 23, 24, 25 and 26 show specific plots for 1%, 5%, 10%, and 15%, respectively. The uncertainty in the temperature readings were also found the same way, and are presented in the listed figures.

## VIII. CONCLUSIONS

The values of the effective emissivity needed to bring the temperature reading of an optical pyrometer into agreement with the temperature measured by a thermocouple were measured under different experimental conditions. The objects used included a mug of hot water, soldering iron and a heatable sample holder for a scanning Auger microprobe (SAM). Preliminary experiments were done on the bench and the pyrometer was then calibrated in-situ in the SAM. The emissivity of the sample holder was increased by placing black carbon tape on the surface during the bench calibration, and by painting the surface black for the SAM tests. The limited spectral transmission of the ZnSe lens and viewport were compensated by setting the pyrometer effective emissivity so that the pyrometer reading matched the thermocouple. The field of view of the pyrometer at the location of the sample holder was found to be 0.6 cm in diameter, and was larger than the projected area the sample holder in the SAM. The effect of cold objects in the field of view was also compensated by adjusting the effective emissivity. Small metallic (reflective) objects will be studied in the SAM lithium wetting experiments. The

effect of small metallic objects was studied and it was found that value of the percent change in effective emissivity was only a few percent higher than the value of area percentage itself (for a metal tab covering 10% of the area, the effective emissivity will decrease by about 10%). When the pyrometer was installed on the SAM, it was found that the effective emissivity of the setup changed slightly with the sample holder temperature. The change was the result of the transmission losses through the ZnSe and the changing temperature differential between the sample holder and the colder background objects. We conclude that with the appropriate setting of the effective emissivity from Fig. 21, the pyrometer can track the SAM sample temperature to within 20%. The large uncertainties on these calculated values were a product of the large uncertainties in the data fitting process, which was necessary to find continuous relationships between the current, temperature and emissivity, but it is possible that these uncertainties could be reduced, and the predictions more accurate, with more precise experiments.

## **IX. Acknowledgments**

This work was made possible by funding from the Department of Energy for the Summer Undergraduate Laboratory Internship (SULI) program. This work is supported by the US DOE Contract No.DE-AC02-09CH11466.

## List of Figures:

**Figure 1.** Pyrometer digital readout

**Figure 2.** Pyrometer with laser alignment attachment

**Figure 3.** Effect of emissivity setting on temperature reading

**Figure 4.** Experimental setups. Dimensions in cm. The aluminum aperture in (d), explained in Section VI, is attached to the sample holder using plastic screws so as to insulate the aluminum from the heated sample holder.

**Figure 5.** Difference between pyrometer and thermocouple readings for ZnSe tests with coffee mug

**Figure 6.** Difference between pyrometer and thermocouple readings for ZnSe tests with soldering iron, run with an emissivity setting of  $\epsilon = 0.45$ .

**Figure 7.** Relative sizes of iron tip and field of view. The dashed white line represents the small forward end of the sloped tip

**Figure 8.** Difference between pyrometer and thermocouple readings for temperature dependence test with soldering iron

**Figure 9.** Location of alignment laser spot for properly aligned pyrometer for sample holder at a  $30^\circ$  angle to the optical axis.

**Figure 10.** Results of field of view test with sample holder at  $30^\circ$  angle to optical axis

**Figure 11.** Temperature along the vertical center for the sample holder. The field of view estimate is shown in dashed lines.

**Figure 12.** Temperature readings as a function of distance for the sample holder at a  $60^\circ$  angle to the optical axis

**Figure 13.** Temperature readings as a function of distance the sample holder at a  $30^\circ$  angle to the optical axis

**Figure 14.** Field of view and projected area of sample holder

**Figure 15.** Pyrometer temperature reading distribution over face of sample holder. Temperatures are in  $^\circ\text{C}$ .

**Figure 16.** Effect of pyrometer emissivity setting on pyrometer temperature reading. Each line represents a certain percentage of the sample holder face covered with metal. The areas were as follows: 11% was  $0.09\text{cm}^2$ ; 15% was  $0.12\text{cm}^2$ ; 38% was  $0.30\text{cm}^2$ . The average thermocouple reading for this test was  $114^\circ\text{C}$ .

**Figure 17.** Effective emissivity as a function of area covered by metal for a sample holder temperature of  $114^\circ\text{C}$ . The dashed line is the exponential fit found with Excel (Eq. 3).

**Figure 18.** Sample holder temperature, as measured by the thermocouple, as a function of time for each current value.

**Figure 19** Equilibrium sample holder temperature as a function of current.

**Figure 20.** Effective emissivity of sample holder in SAM setup as a function of temperature. The solid line shows the logarithmic fit found with Excel.

**Figure 21.** Effective emissivity of the sample holder as a function of current for the SAM setup

**Figure 22.** Sample holder with no metal; pyrometer emissivity setting with uncertainty, and percent uncertainty in the pyrometer temperature reading.

**Figure 23.** One percent of sample holder surface covered in metal; pyrometer emissivity setting with uncertainty, and percent uncertainty in the pyrometer temperature reading.

**Figure 24.** Five percent of sample holder surface covered in metal; pyrometer emissivity setting with uncertainty, and percent uncertainty in the pyrometer temperature reading.

**Figure 25.** Ten percent of sample holder surface covered in metal; pyrometer emissivity setting with uncertainty, and percent uncertainty in the pyrometer temperature reading.

**Figure 26.** Fifteen percent of sample holder surface covered in metal; pyrometer emissivity setting with uncertainty, and percent uncertainty in the pyrometer temperature reading.

## REFERENCES

- [1] J. W. Coenen et al., Phys. Scr. T159 (2014) 014037
- [2] E. Klein, B. Schwarz, C. Eisenmenger-Sittner, C. Tomastik, P.B. Barna, A. Kovács, Vacuum 2005; 80:74-80
- [3] E Saiz, A Tomsia, Nature Materials 2004;3:903-909
- [4] C.H. Skinner, A.M. Capece, J.P. Rozell, B.E. Koel ‘*Spreading of lithium on a stainless steel surface at room temperature*’ J. Nucl. Mater. 468 (2016) 26
- [5] Edmund Optics. <http://www.edmundoptics.com/optics/optical-lenses/plano-convex-pcx-spherical-singlet-lenses/zinc-selenide-plano-convex-pcx-lenses/47074/>.
- [6] Omega. OS550A/OS550AM/OS550A-BB Series Industrial Infrared Thermometer/Transmitter User’s Guide.
- [7] Electro-Optical Industries. [http://www.electro-optical.com/eoi\\_page.asp?h=Emissivity%20of%20Materials](http://www.electro-optical.com/eoi_page.asp?h=Emissivity%20of%20Materials)
- [8] Cole-Parmer. <http://www.coleparmer.com/TechLibraryArticle/254#anchor63>

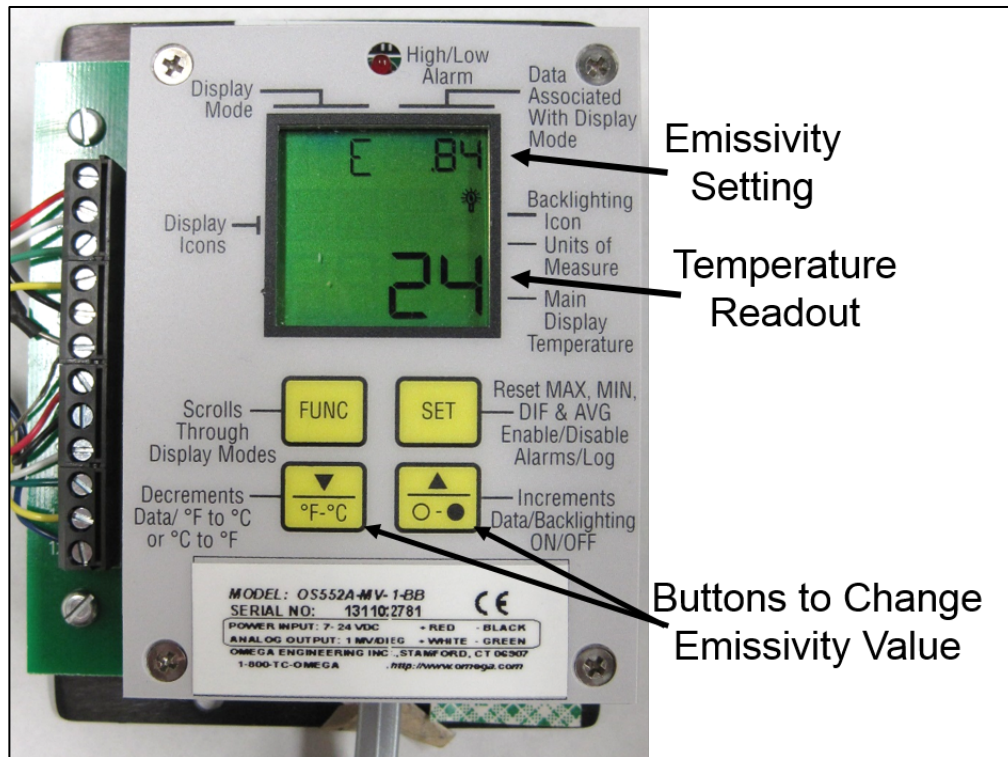


**Figure 1.** Pyrometer digital readout

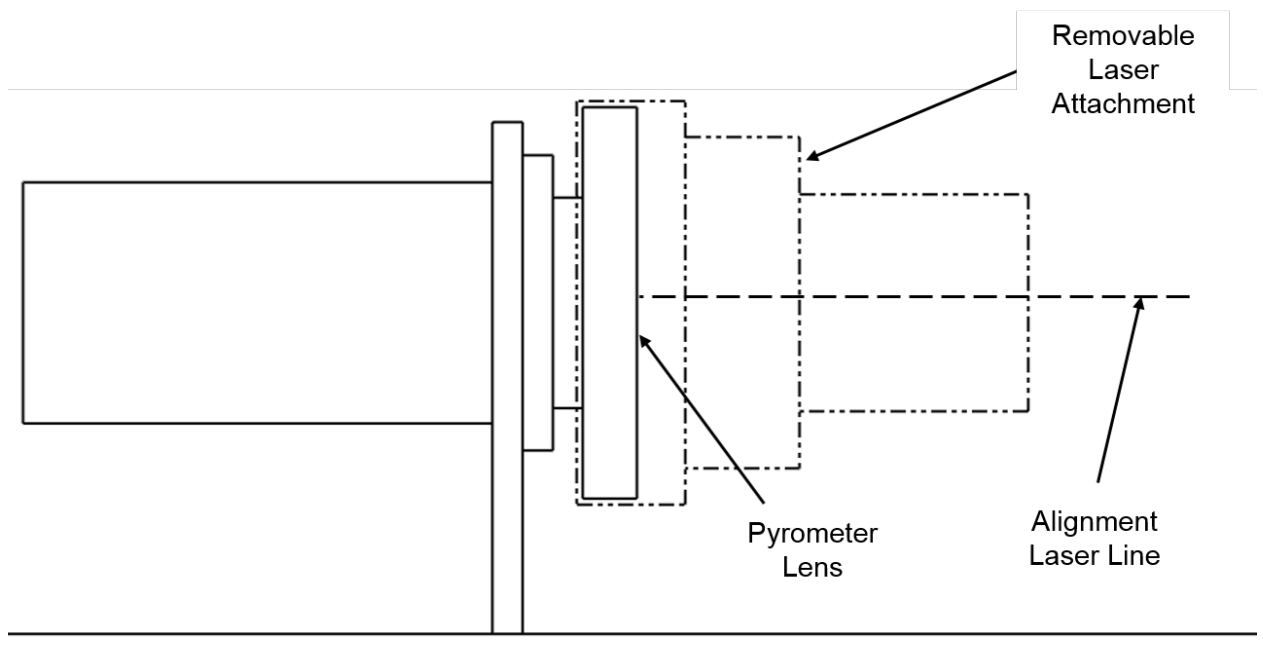


**Figure 2.** Pyrometer with laser alignment attachment

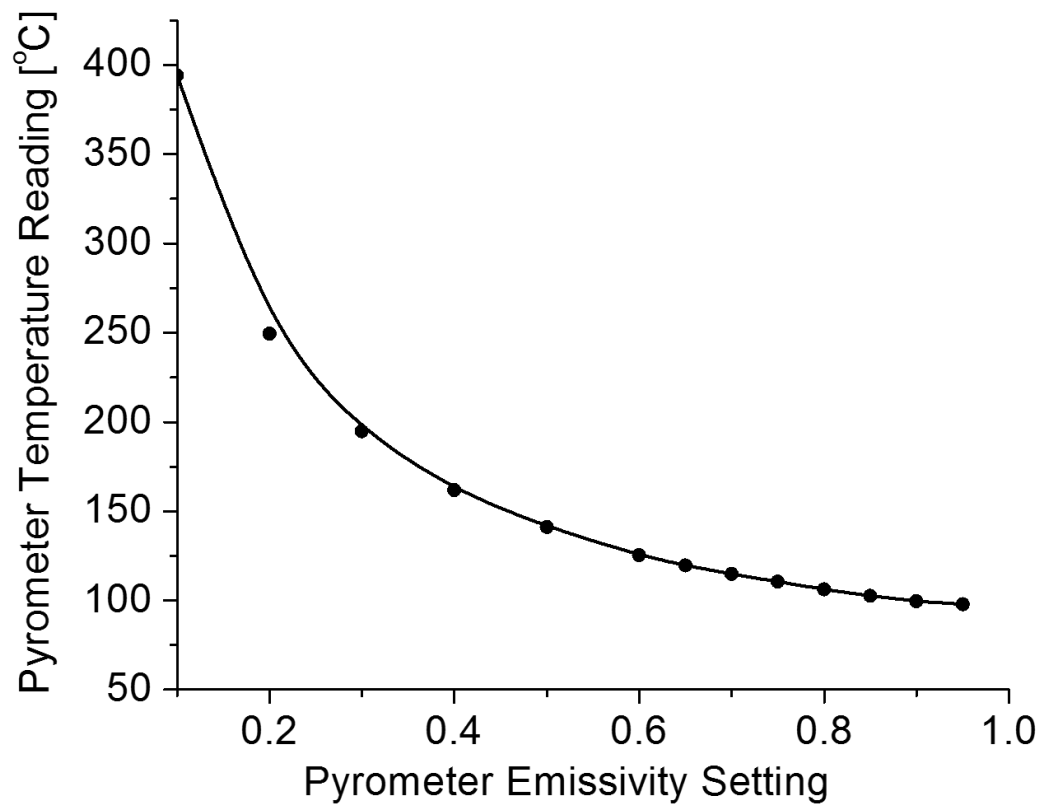


**Figure 3.** Effect of emissivity setting on temperature reading

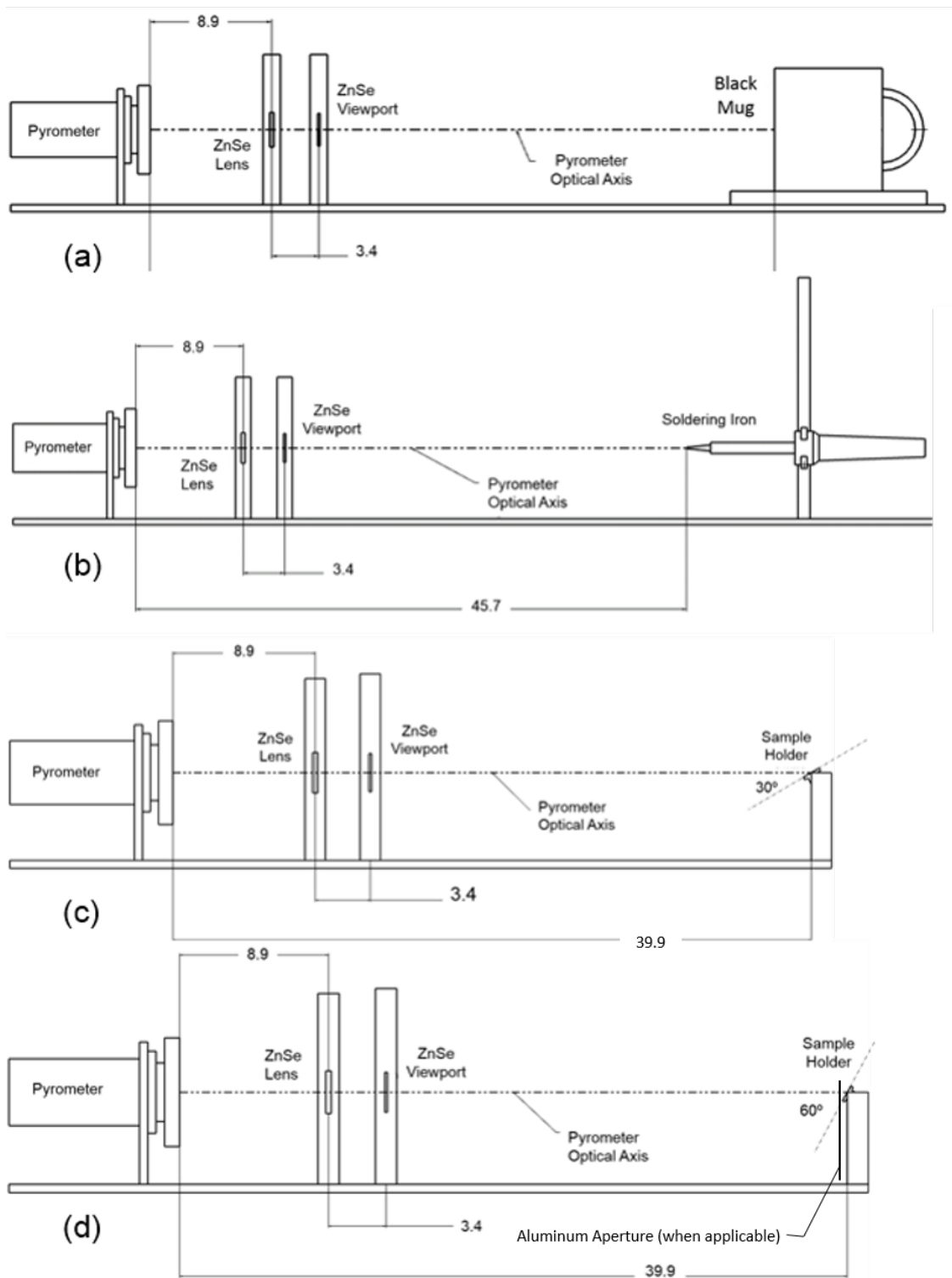


**Figure 4.** Experimental setups. Dimensions in cm. The aluminum aperture in (d), explained in Section VI, is attached to the sample holder using plastic screws so as to insulate the aluminum from the heated sample holder.

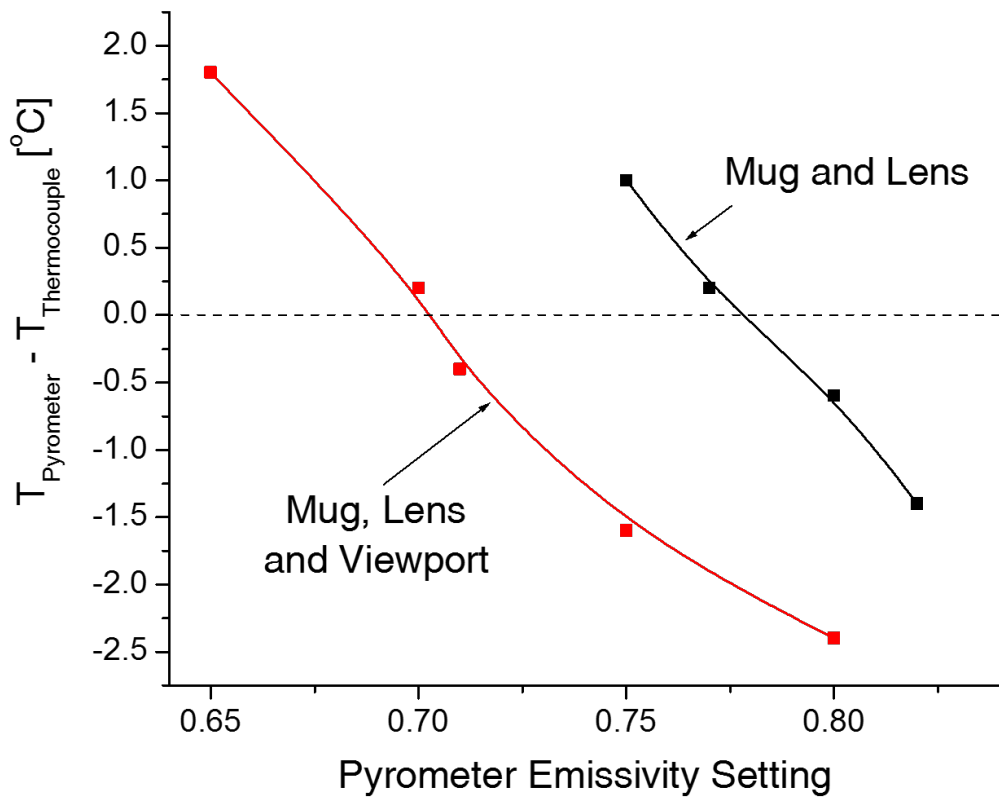


**Figure 5.** Difference between pyrometer and thermocouple readings for ZnSe tests with coffee mug

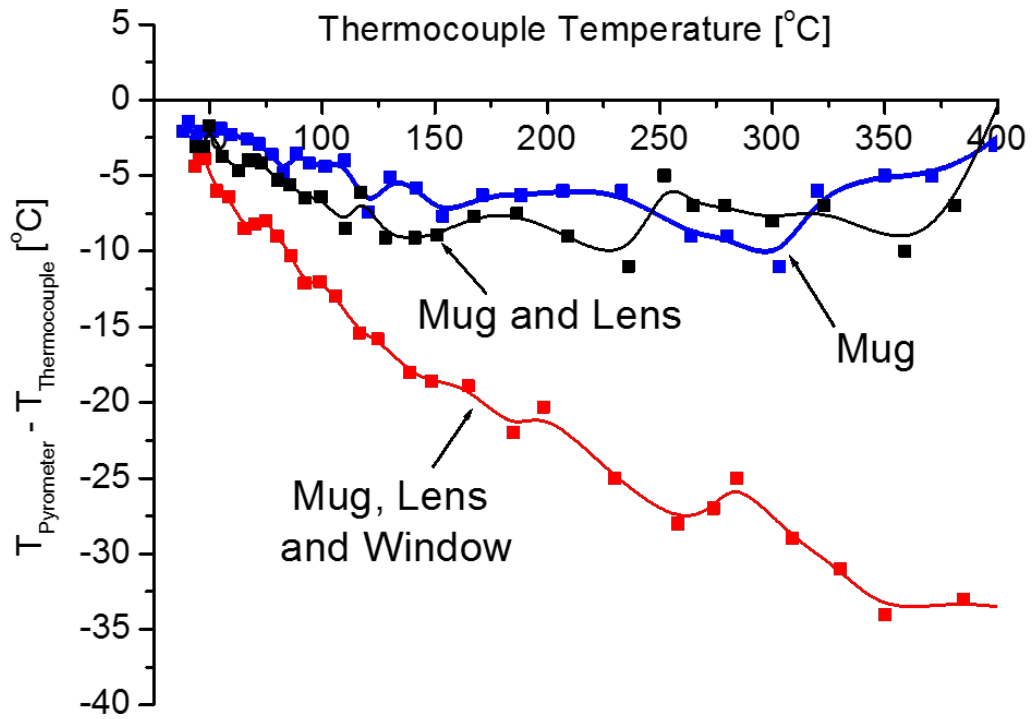


**Figure 6.** Difference between pyrometer and thermocouple readings for ZnSe tests with soldering iron, run with an emissivity setting of  $\epsilon = 0.45$ .

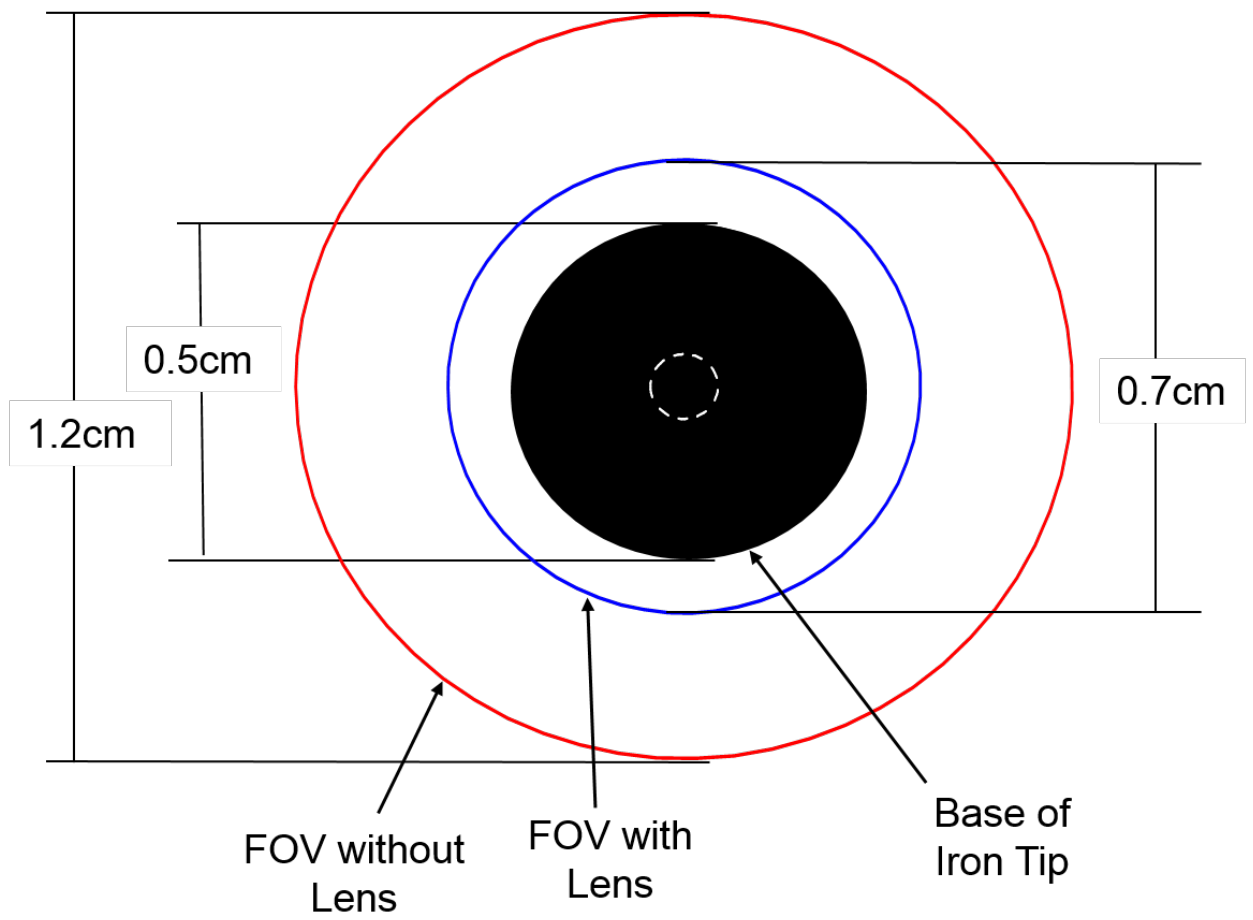


**Figure 7.** Relative sizes of iron tip and field of view. The dashed white line represents the small forward end of the sloped tip

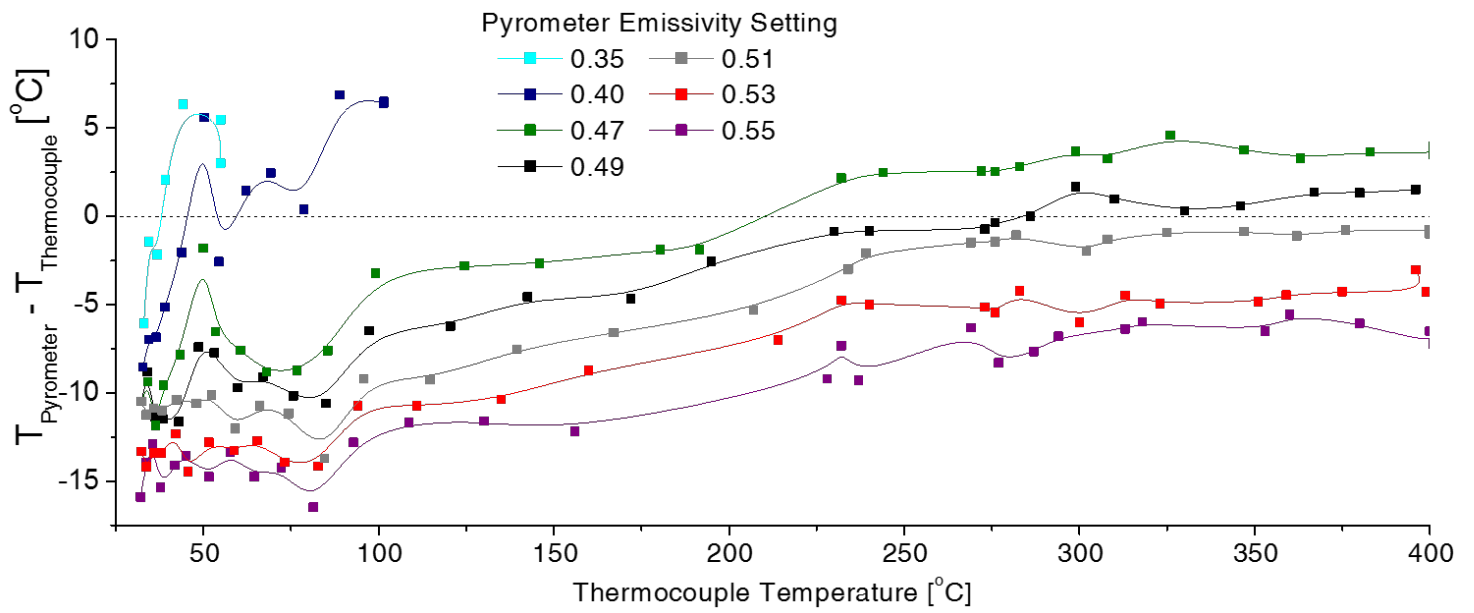


**Figure 8.** Difference between pyrometer and thermocouple readings for temperature dependence test with soldering iron

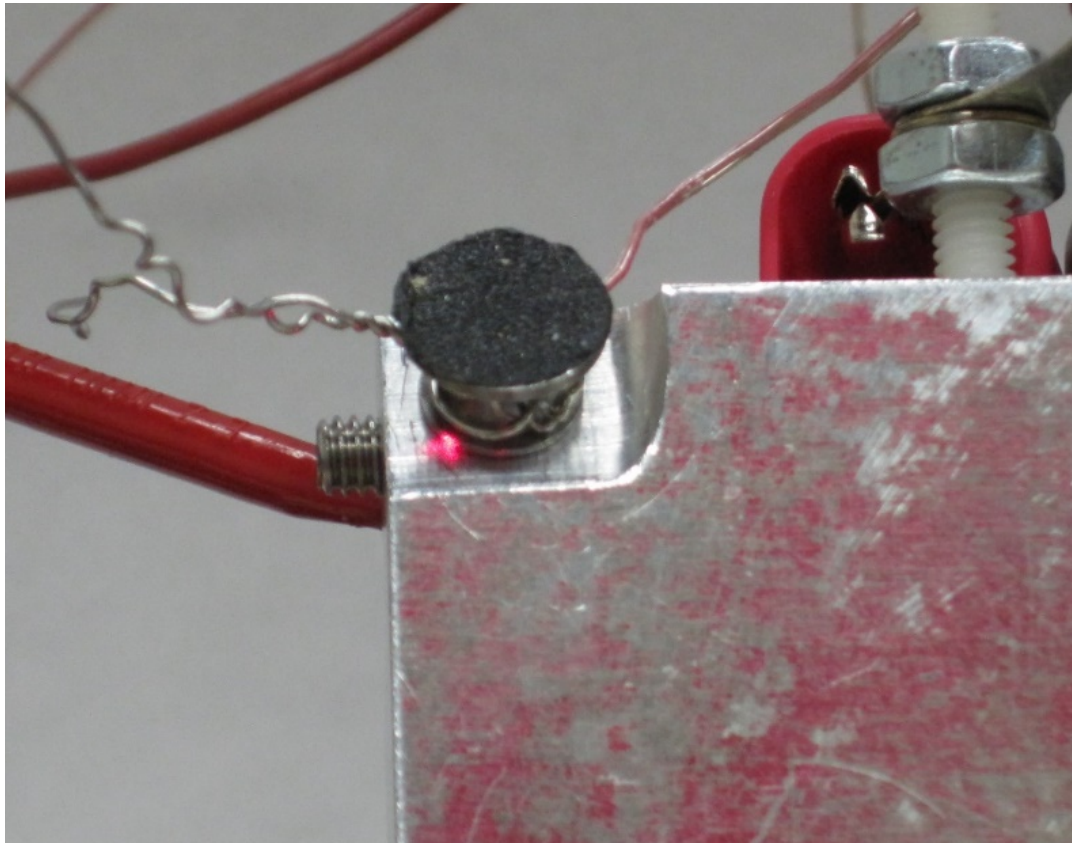


**Figure 9.** Location of alignment laser spot for properly aligned pyrometer for sample holder at a  $30^\circ$  angle to the optical axis.

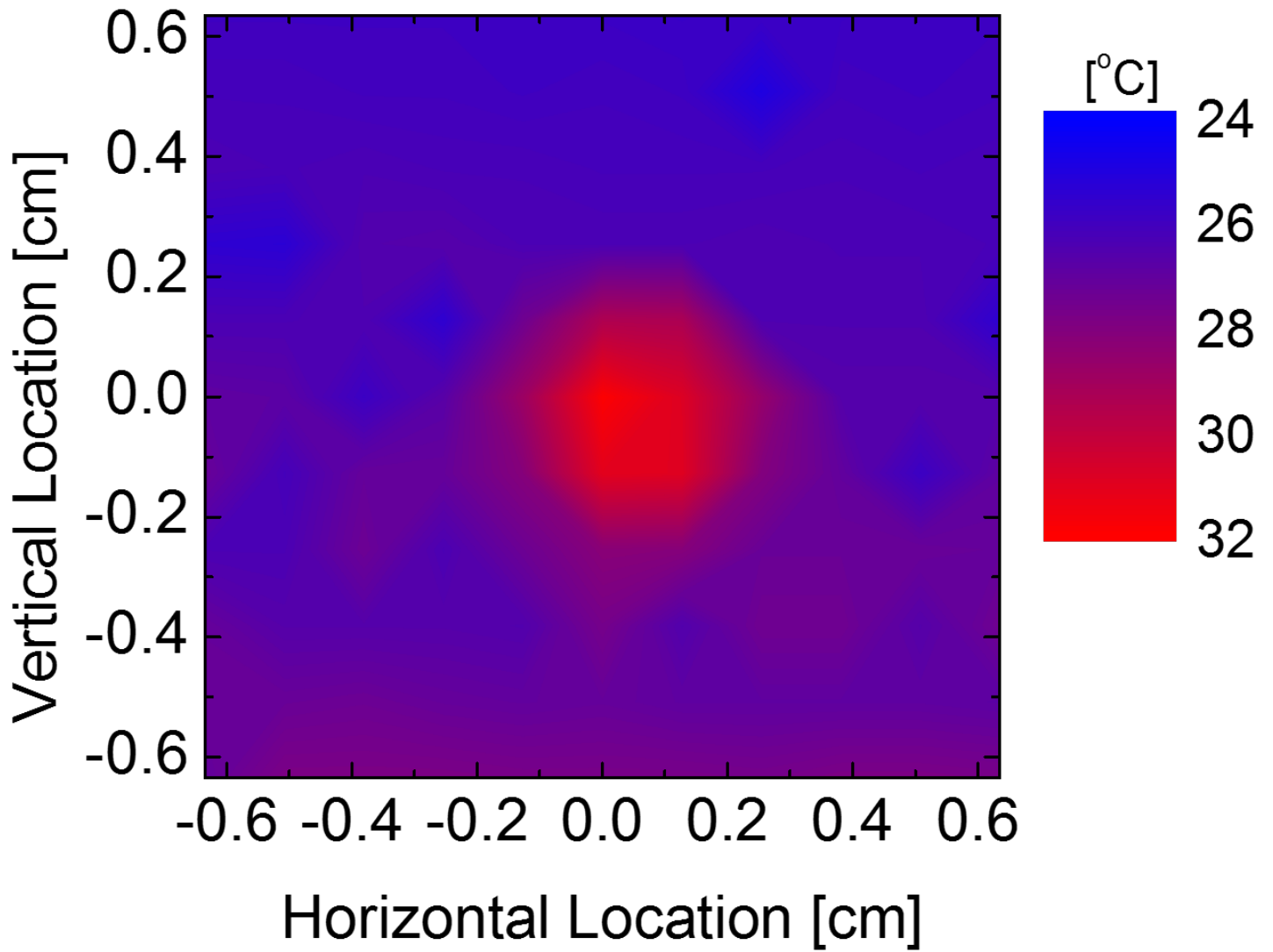


**Figure 10.** Results of field of view test with sample holder at 30° angle to optical axis

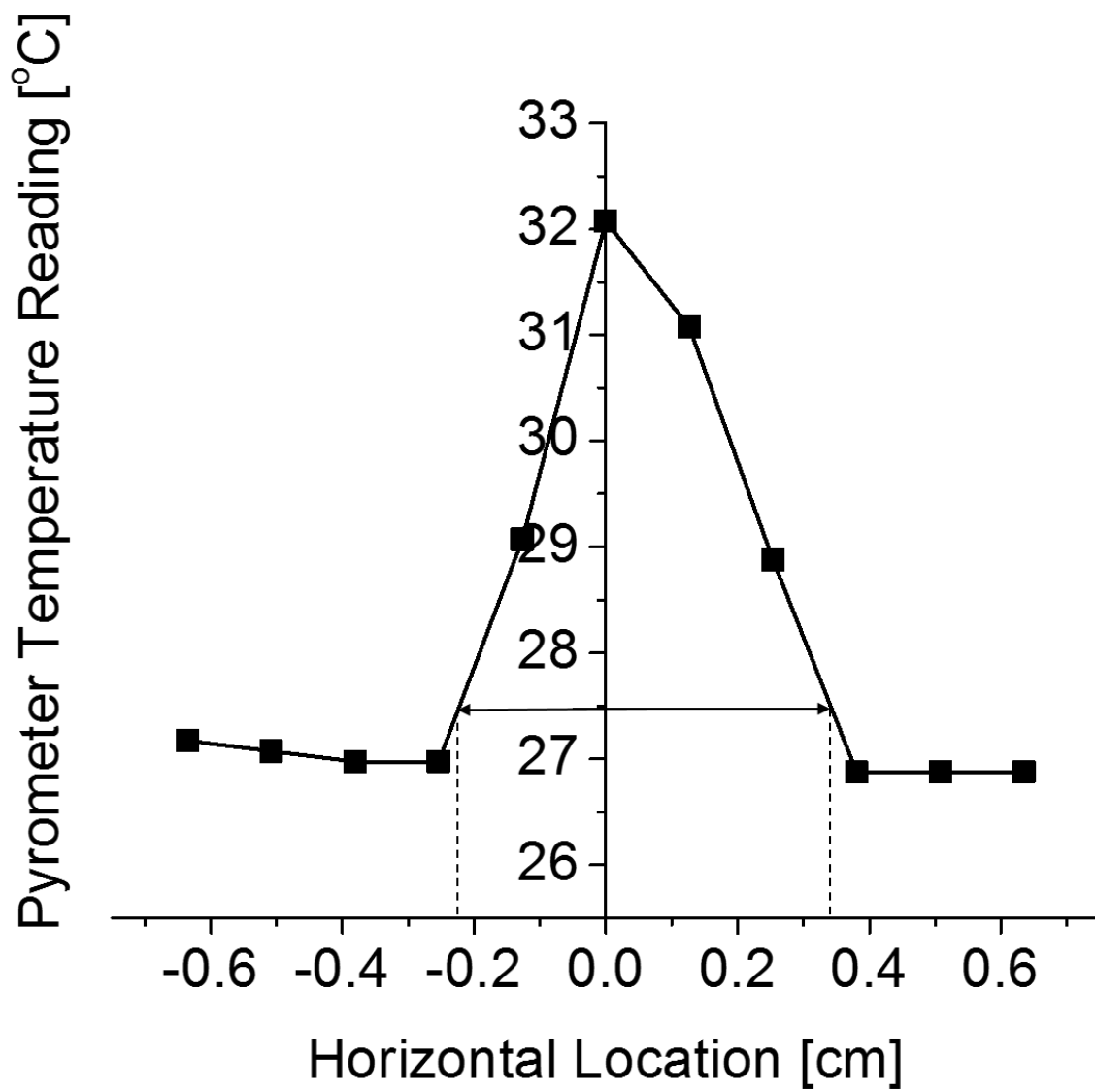


**Figure 11.** Temperature along the vertical center for the sample holder. The field of view estimate is shown in dashed lines.

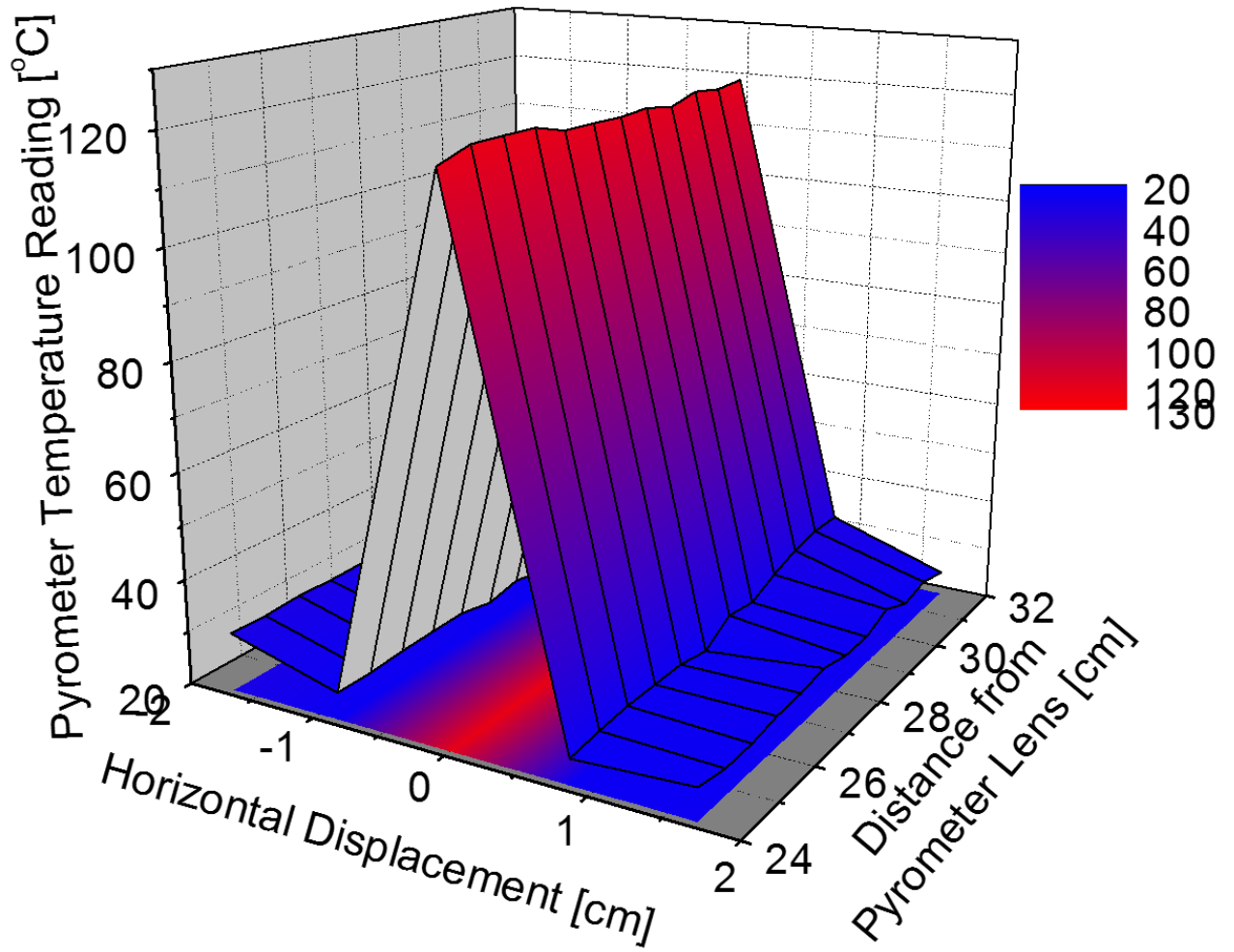


**Figure 12.** Temperature readings as a function of distance for the sample holder at a 60° angle to the optical axis

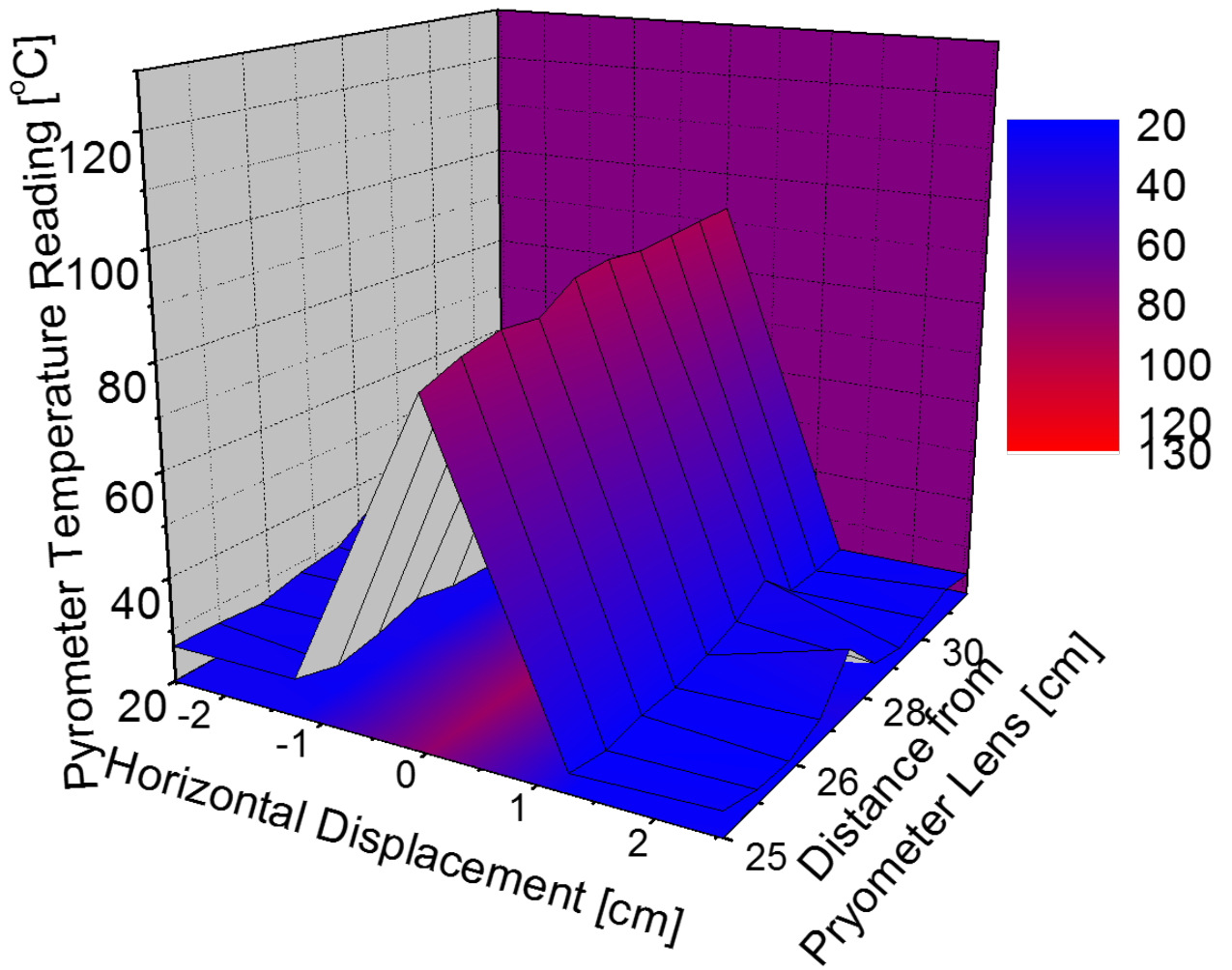


**Figure 13.** Temperature readings as a function of distance the sample holder at a 30° angle to the optical axis

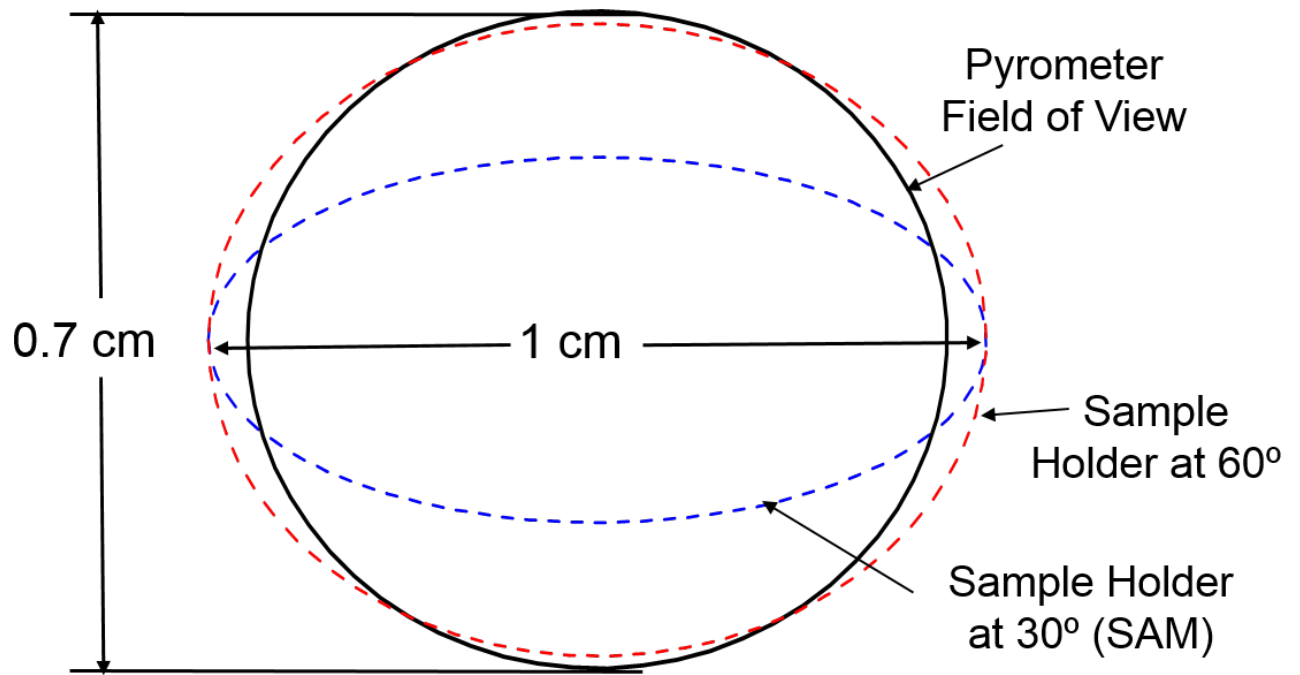


**Figure 14.** Field of view and projected area of sample holder

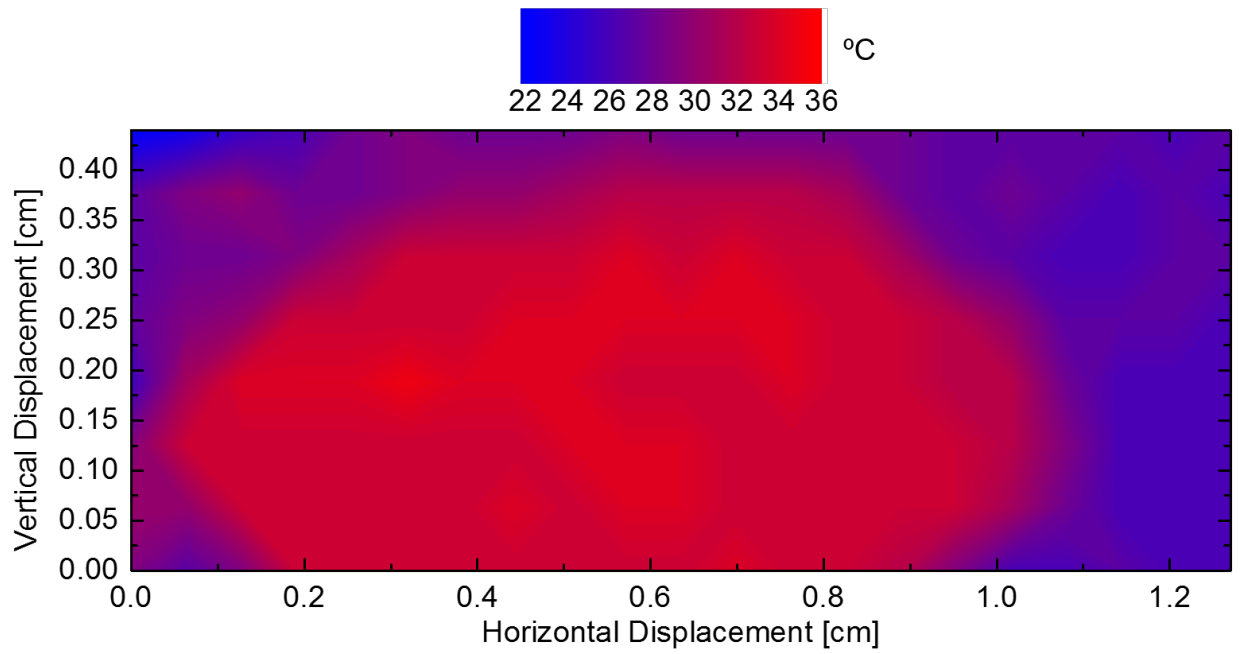


**Figure 15.** Pyrometer temperature reading distribution over face of sample holder. Temperatures are in °C.

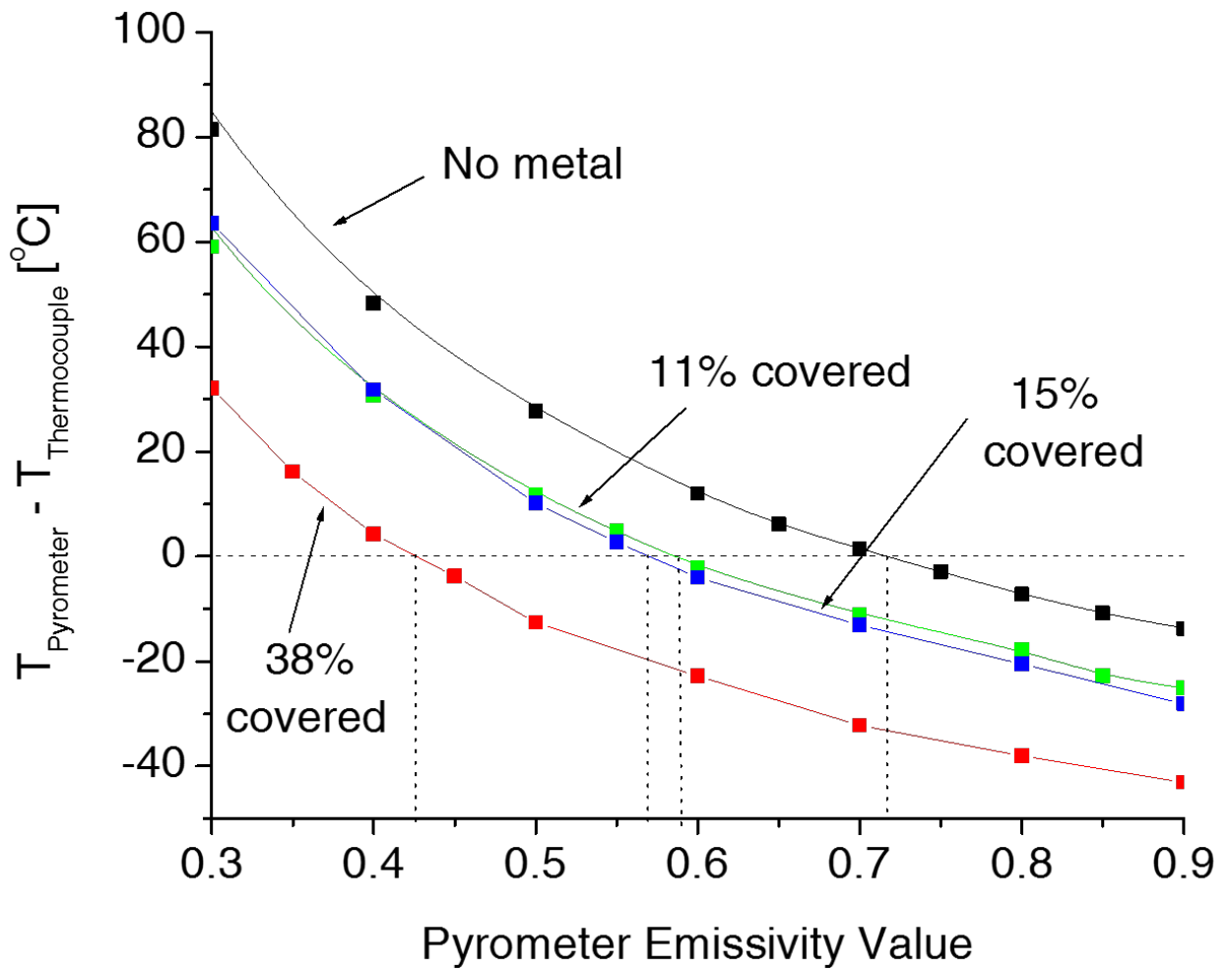


**Figure 16.** Effect of pyrometer emissivity setting on pyrometer temperature reading. Each line represents a certain percentage of the sample holder face covered with metal. The areas were as follows: 11% was 0.09cm<sup>2</sup>; 15% was 0.12cm<sup>2</sup>; 38% was 0.30cm<sup>2</sup>. The average thermocouple reading for this test was 114°C.

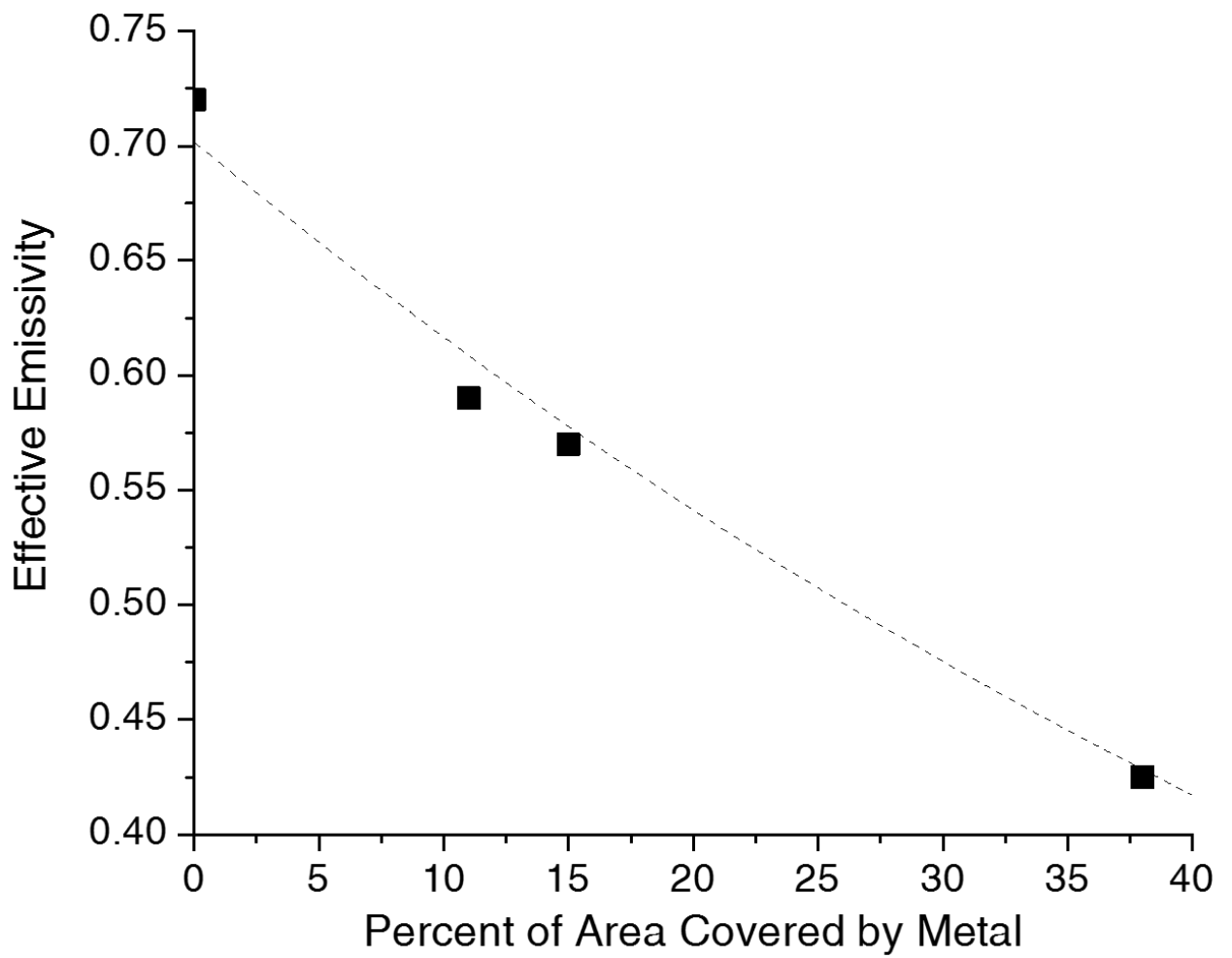


**Figure 17** Effective emissivity as a function of area covered by metal for a sample holder temperature of 114°C. The dashed line is the exponential fit found with Excel (Eq. 3).

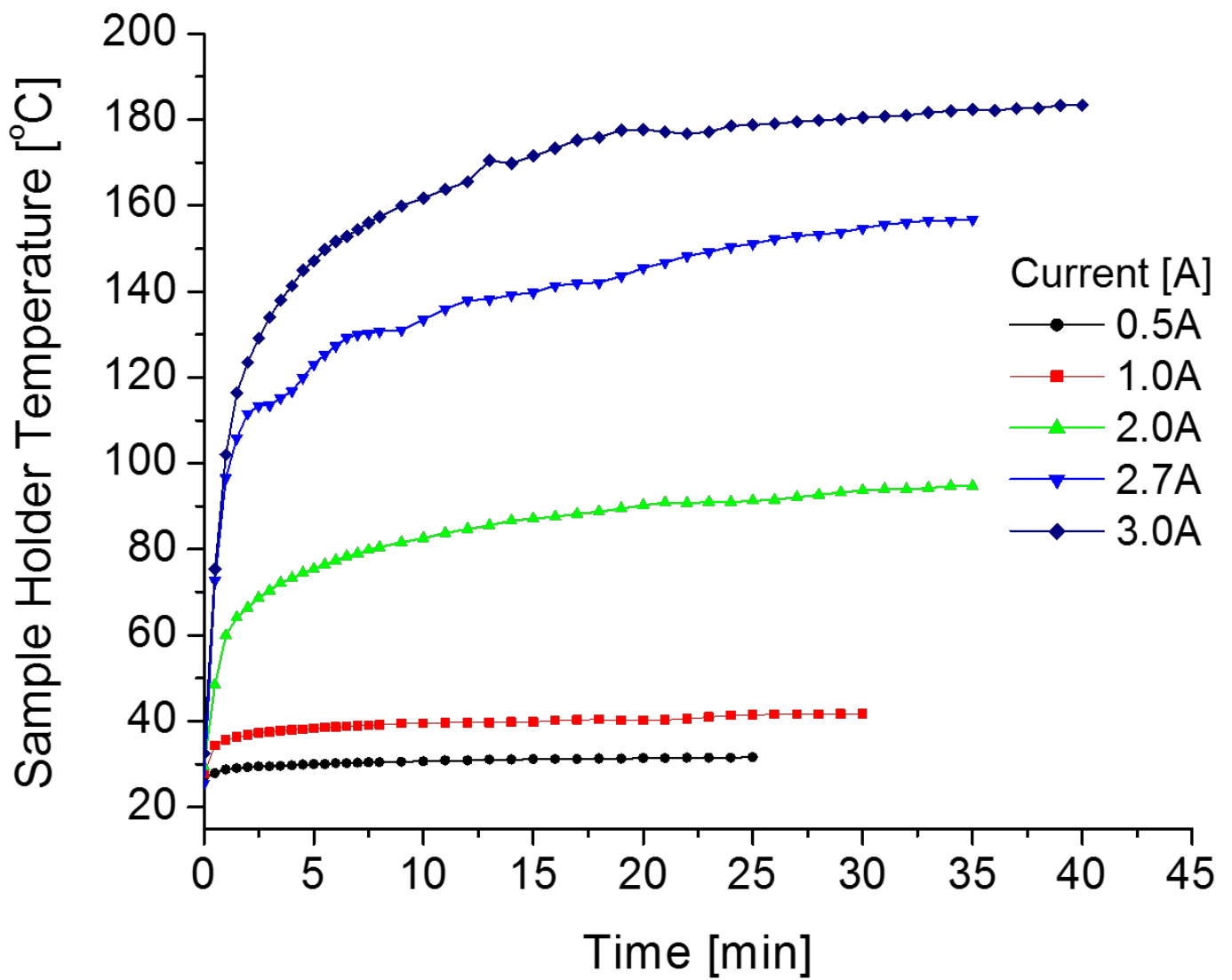


**Figure 18.** Sample holder temperature, as measured by the thermocouple, as a function of time for each current value.

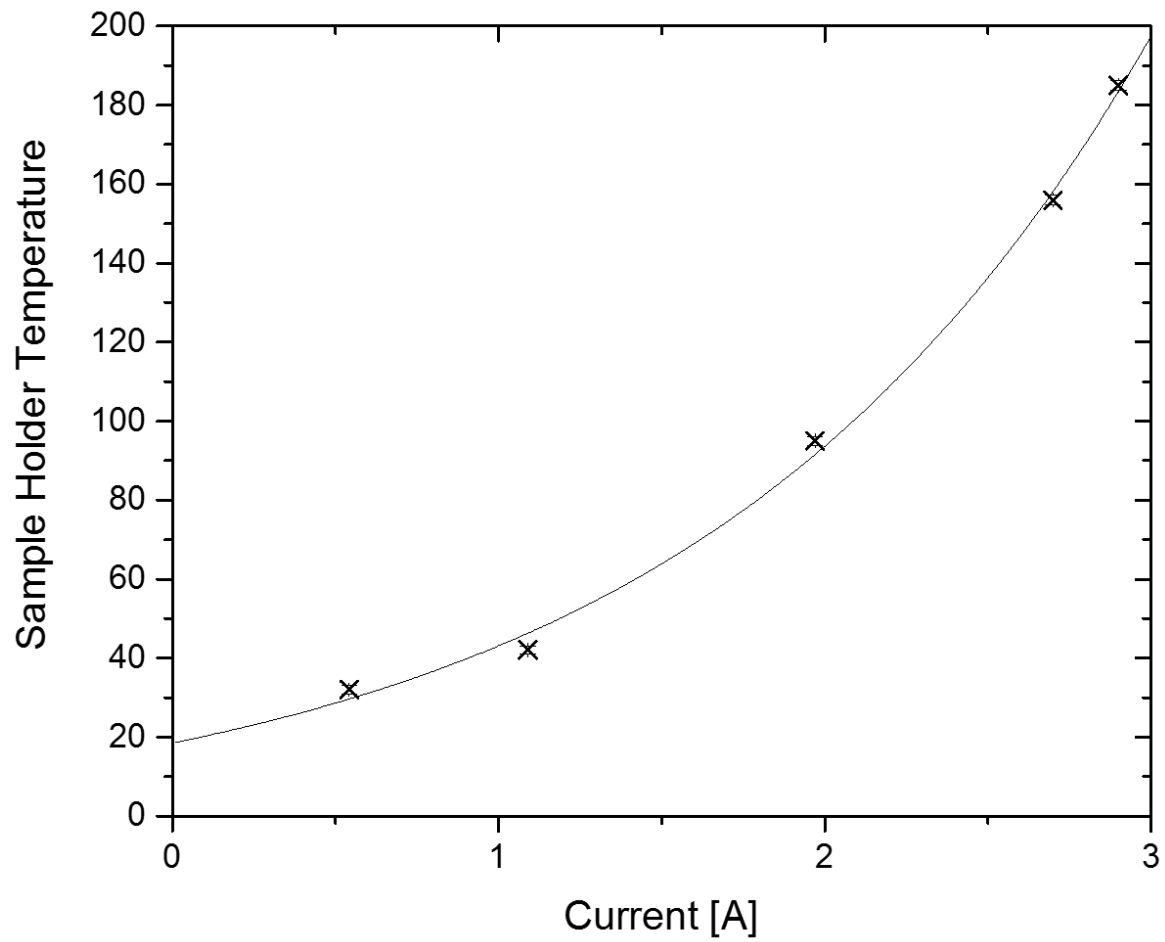


**Figure 19** Equilibrium sample holder temperature as a function of current.

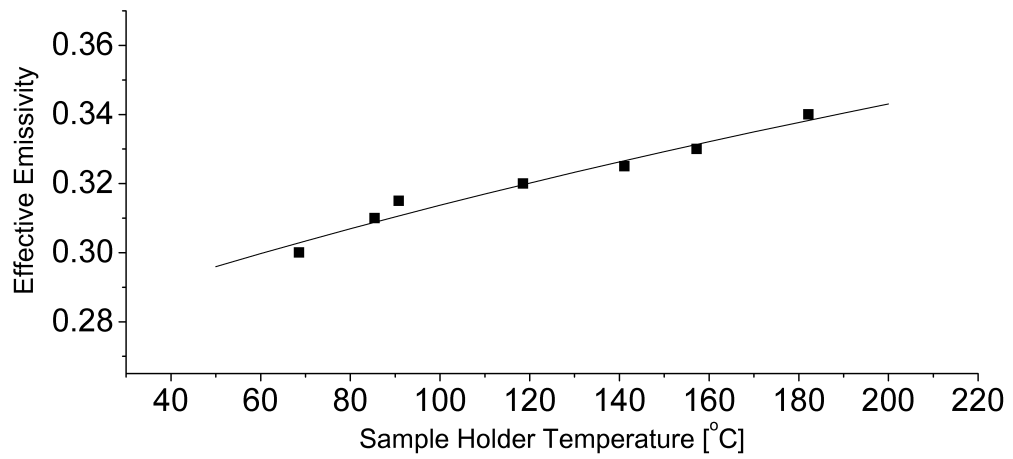


**Figure 20.** Effective emissivity of sample holder in SAM setup as a function of temperature. The solid line shows the logarithmic fit found with Excel.

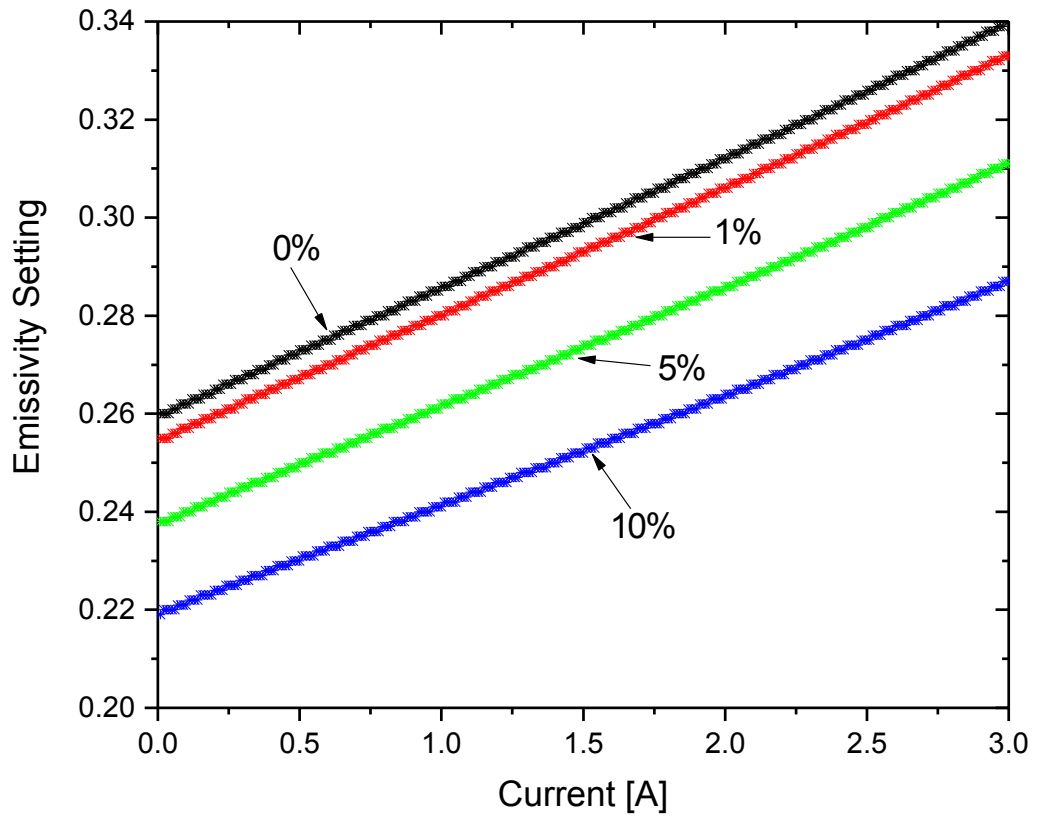


**Figure 21.** Effective emissivity of the sample holder as a function of current for the SAM setup

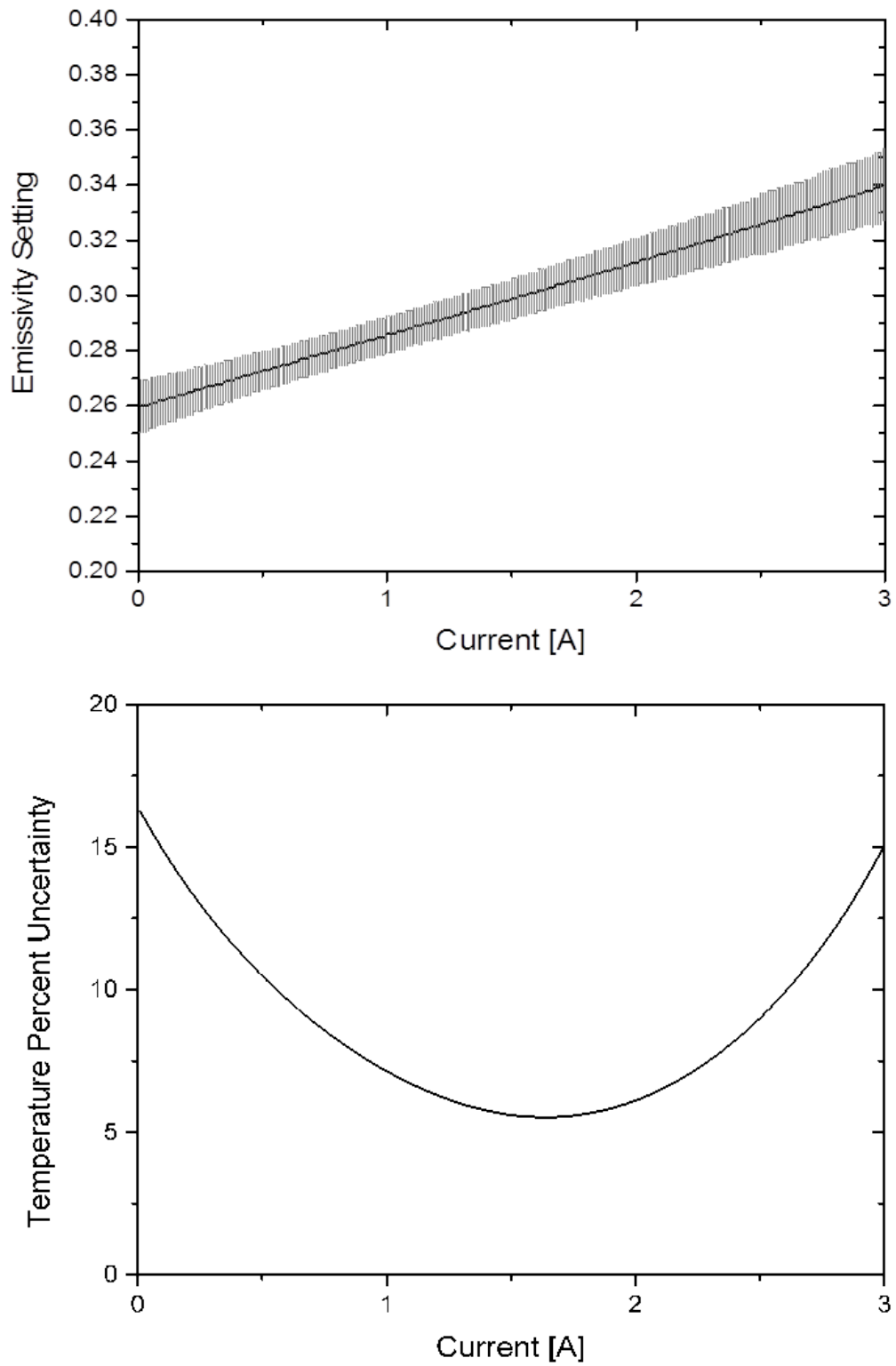


**Figure 22.** Sample holder with no metal; pyrometer emissivity setting with uncertainty, and percent uncertainty in the pyrometer temperature reading.

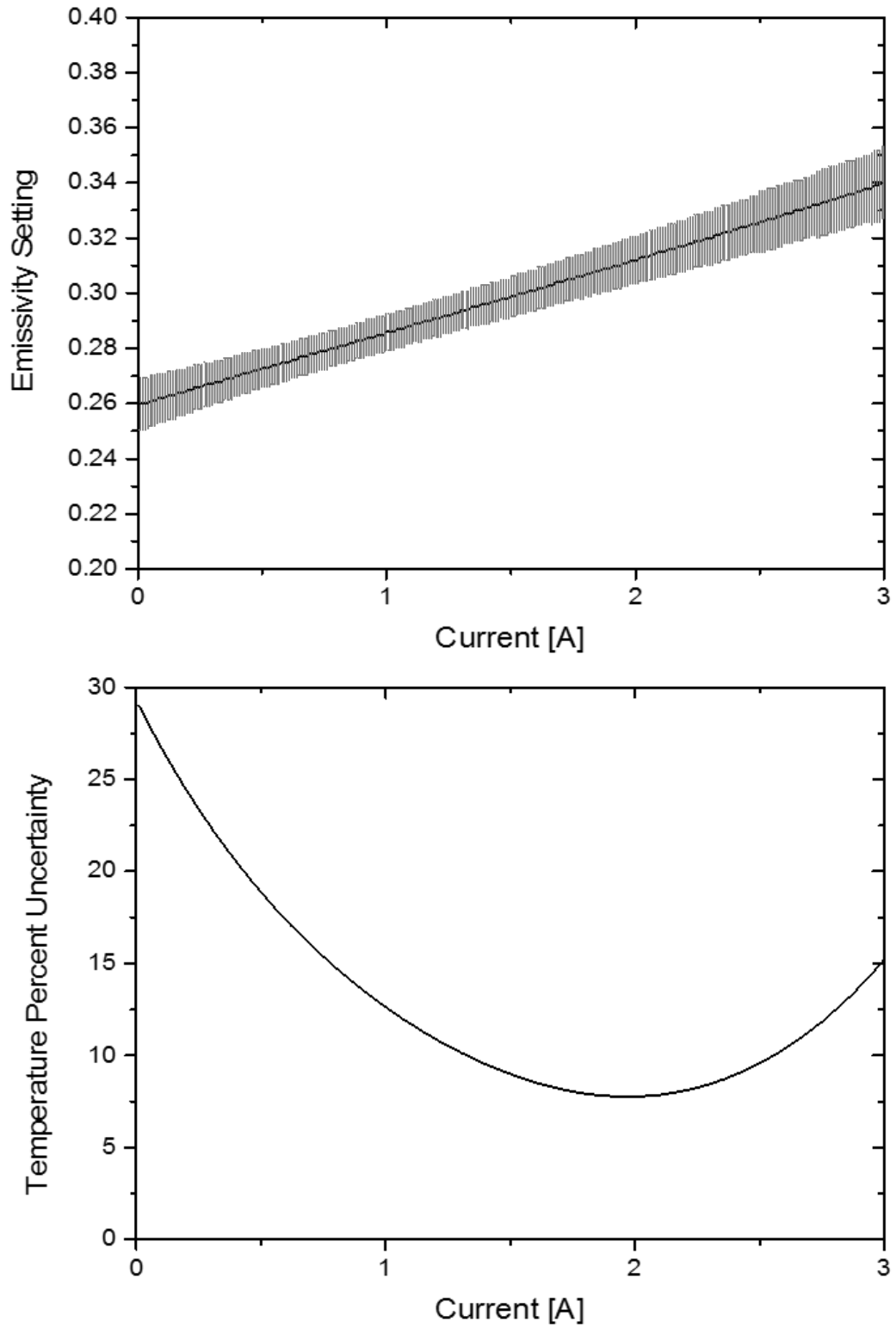


**Figure 23.** One percent of sample holder surface covered in metal; pyrometer emissivity setting with uncertainty, and percent uncertainty in the pyrometer temperature reading.

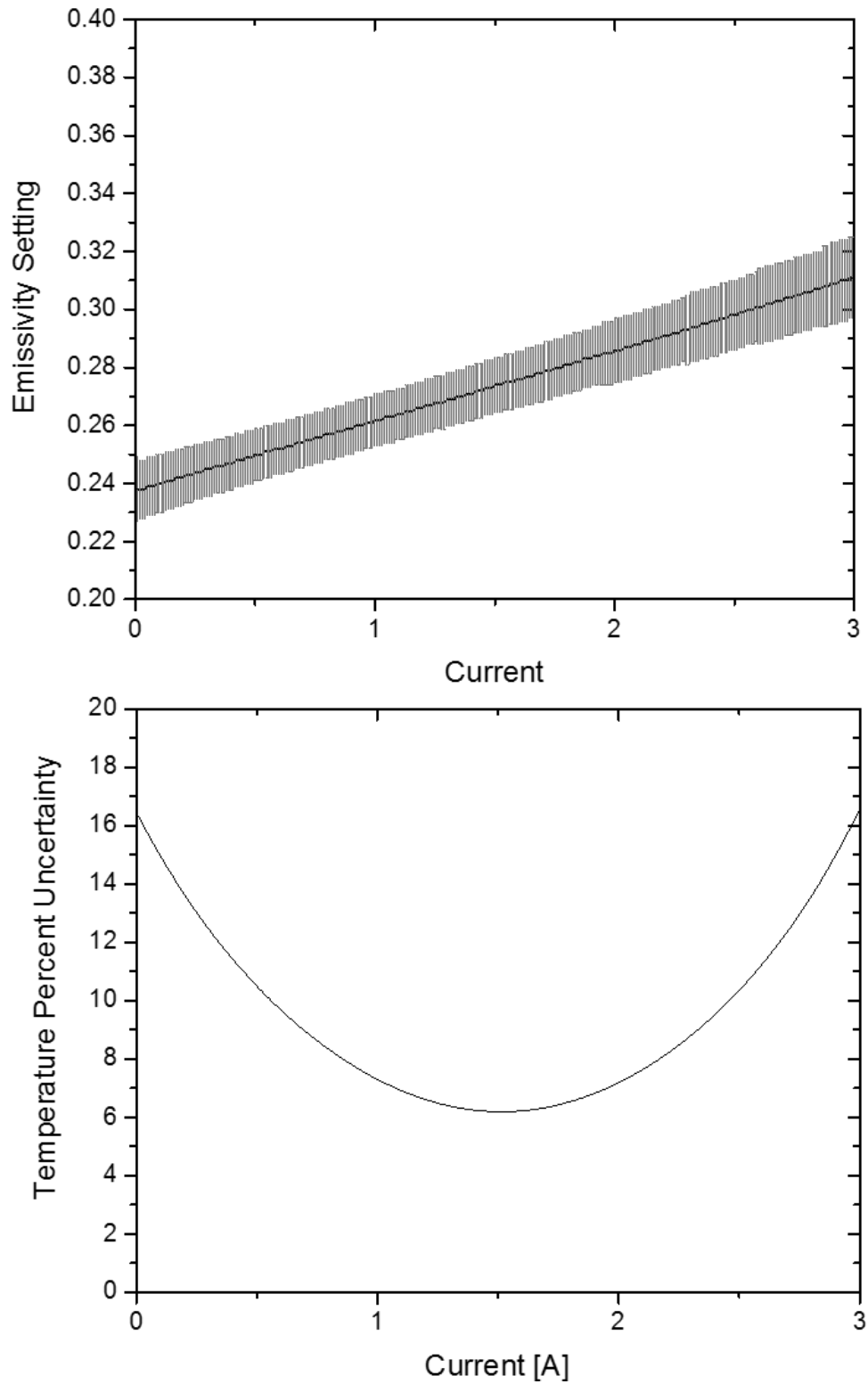


**Figure 24.** Five percent of sample holder surface covered in metal; pyrometer emissivity setting with uncertainty, and percent uncertainty in the pyrometer temperature reading.

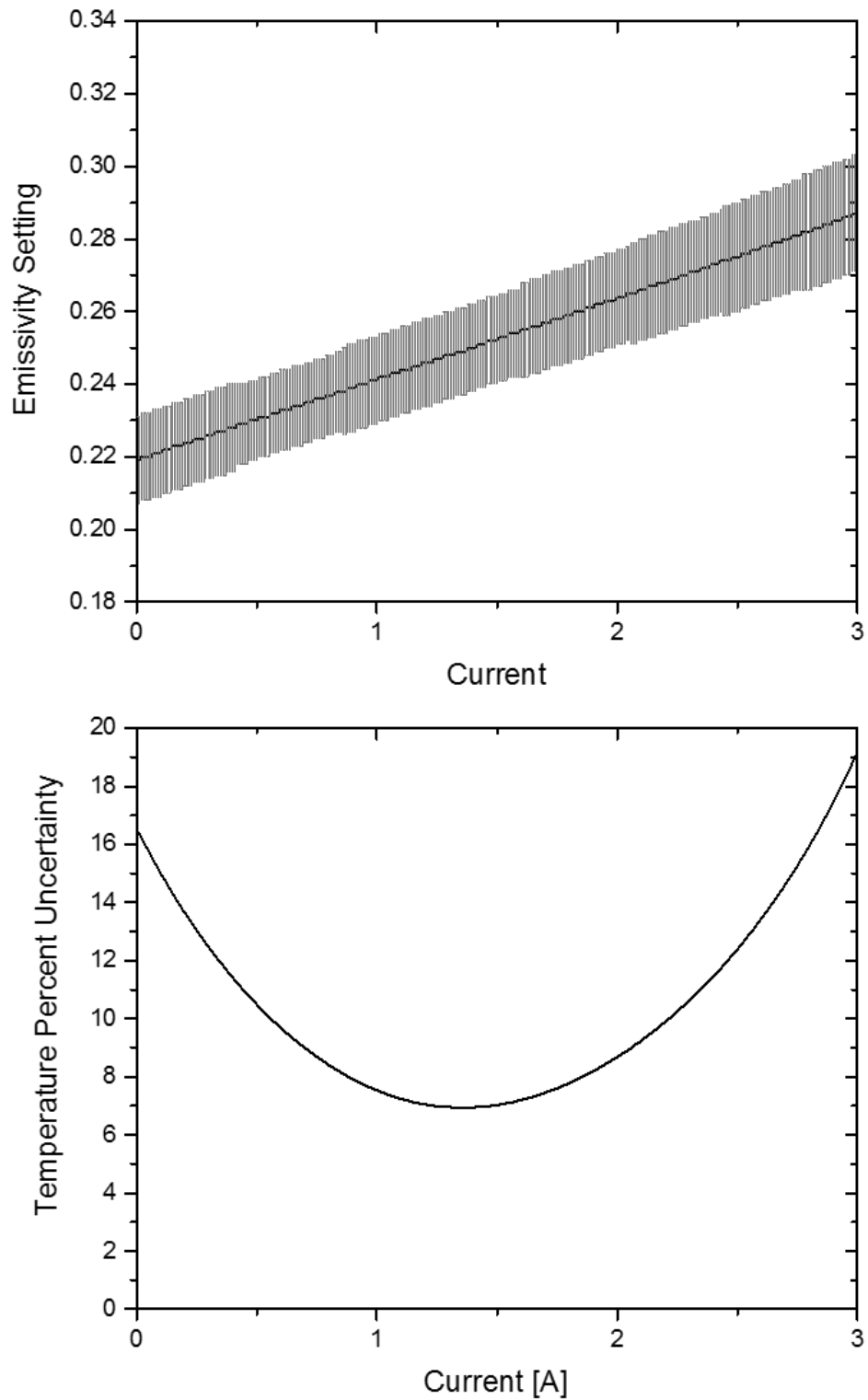


**Figure 25.** Ten percent of sample holder surface covered in metal; pyrometer emissivity setting with uncertainty, and percent uncertainty in the pyrometer temperature reading.

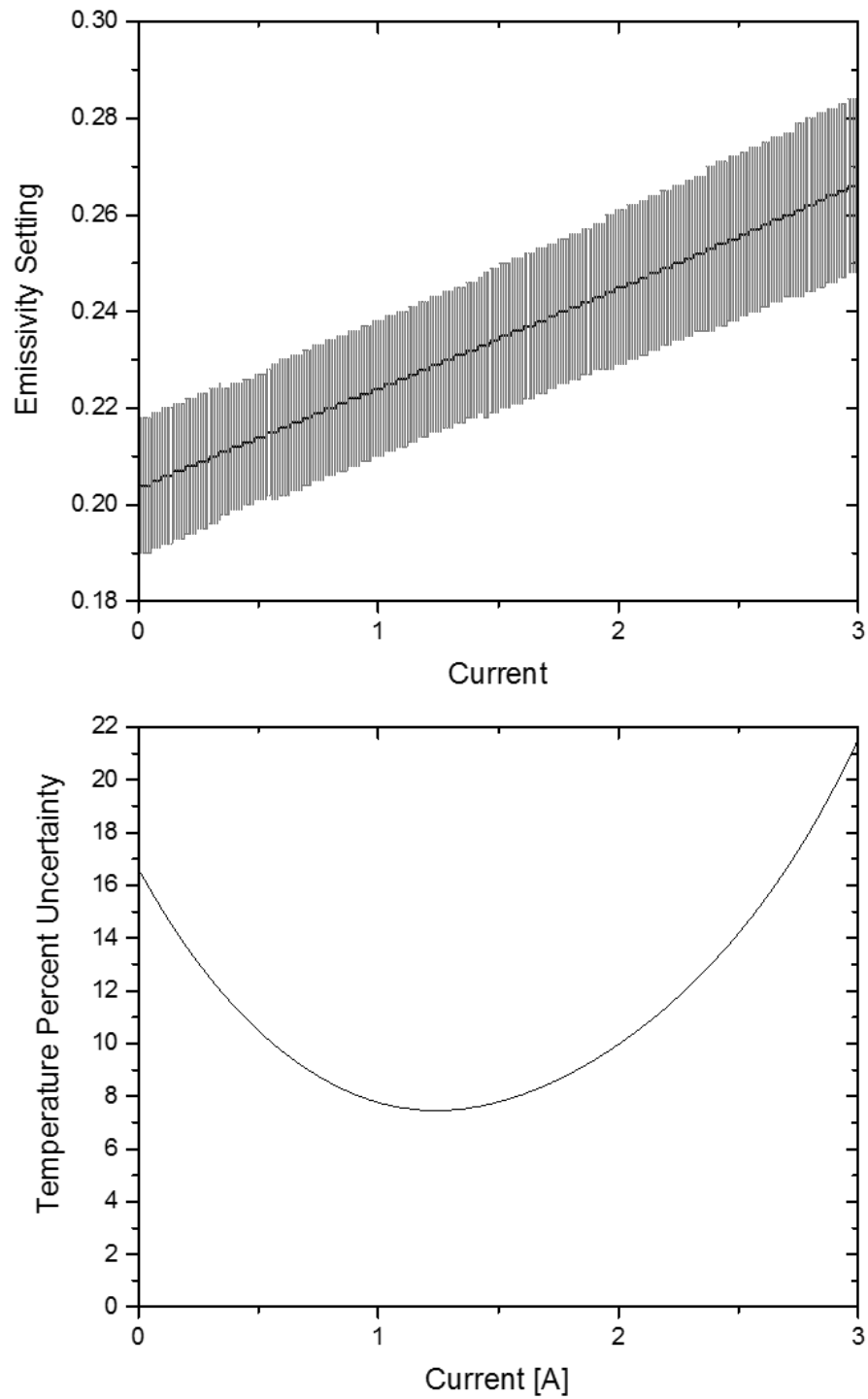


**Figure 26.** Fifteen percent of sample holder surface covered in metal; pyrometer emissivity setting with uncertainty, and percent uncertainty in the pyrometer temperature reading.

# Princeton Plasma Physics Laboratory Office of Reports and Publications

Managed by  
Princeton University

under contract with the  
U.S. Department of Energy  
(DE-AC02-09CH11466)

---

P.O. Box 451, Princeton, NJ 08543  
Phone: 609-243-2245  
Fax: 609-243-2751

E-mail: [publications@pppl.gov](mailto:publications@pppl.gov)

Website: <http://www.pppl.gov>